

UNIVERSITY OF CALIFORNIA
Davis

Study of the Upsilon resonances with the CMS
detector

A Dissertation submitted in partial satisfaction
of the requirements for the degree of

Doctor of Philosophy

in

Physics

by

Guillermo Breto Rangel

Committee in Charge:

Professor Manuel Caldern de la Barca Snchez, Chair

Daniel Cebra, Ph. D.

Ramona Voigt

July 2013

The Dissertation of
Guillermo Breto Rangel is approved:

Daniel Cebra, Ph. D.

Ramona Voigt

Professor Manuel Caldern de la Barca Snchez, Committee Chairperson

August 2013

Study of the Upsilon resonances with the CMS detector

Copyright © 2013

by

Guillermo Breto Rangel

To the importance of being.

Acknowledgements

I acknowledge.

Curriculum Vitæ

Guillermo Breto Rangel

Education

- 1789 Master of Science in Computer Science, University of California,
Santa Barbara.
- 1492 Bachelor of Science, Web-Based University of Phoenix.

Experience

- 1999 – 2000 Graduate Research Assistant, University of California, Santa Bar-
bara.

Selected Publications

Me Myself, S. Mart, and A. Nother Advisor: “Cool Paper Title,” In *Proc. IEEE Intl. Conference Cool Papers (ICCP)*, August 2000.

Abstract

Study of the Upsilon resonances with the CMS detector

Guillermo Breto Rangel

This Thesis describes the $Y(nS)$ analysis in PbPb , pPb and pp collisions recorded by CMS during different runs. The present work studies thoroughly the suppression of the excited 2S and 3S states in PbPb collisions, relative to the ground 1S state and to the pp control dataset. For the entire phase space accessible, given by $|y| < 2.0$, $p_T < 50$ GeV/c, 0-100% centrality, we measure the double ratio $Y(2S+3S)/Y(1S)$ in PbPb relative to pp collisions to be $\chi = xx$. The relative suppression is further observed to increase with centrality. For the most central collisions, 0-30%, we measure $\chi = xx$, with a significance of over 5σ (p-value xx). No noticeable dependence of χ on p_T or rapidity is observed. The differential production cross-sections of the ground $Y(1S)$ and excited $Y(2S+3S)$ states are also measured, as a function of the dimuon transverse momentum and collision centrality. The observed $Y(1S)$ suppression is found to be consistent with the reduced feeddown from the suppressed excited Y states.

Professor Manuel Caldern de la Barca Snchez
Dissertation Committee Chair

Contents

Acknowledgements	ix
Curriculum Vitæ	xi
Abstract	xiii
List of Figures	xvii
List of Tables	xxiii
1 Introduction	1
1.1 Heavy Ion Physics	2
1.2 Quarkonia	5
2 Measurments	7
3 Datasets	11
3.0.1 PbPb dimuon trigger and skim	11
3.0.2 pp sample	13
3.0.3 Monte Carlo samples	14
4 Fitting	17
4.0.4 Signal model studies	19
4.0.5 Background model studies	23
4.0.6 Fits to the pp data	26
5 Efficiency	33
6 Upper limits	47

7	Final results	61
7.0.7	Single ratio measurement	62
7.0.8	Centrality dependence	67
7.0.9	Double ratio measurement	73
7.0.10	Kinematic dependences	75
7.0.11	Significance	77
	Bibliography	97
	Appendices	99

List of Figures

1.1	Many-body dynamics of QCD in different physics limits.	3
1.2	Left: The light quark chiral condensate versus the temperature computed in lattice QCD with various number of flavours and values of the u, d, s quark masses. Right: The energy density in QCD with 0, 2 and 3 degenerate quark flavours as well as with two light and one heavier (strange) quarks. The horizontal arrow shows the value of the Stefan-Boltzmann limit for an ideal quark-gluon gas	4
1.3	QCD phase diagram in the $1/x, Q^2$ plane (each circle represents a parton with transverse area $\sim 1/Q^2$ and fraction x of the hadron momentum). The different evolution regimes (DGLAP, BFKL, saturation) are indicated, as well as the saturation scale and geometric scaling curves between the dense and dilute domains	6
3.1	Results from the $95\mu b^{-1}$ dataset. (> 3.5)	16
4.1	Fit to the dimuon invariant-mass distributions, for the PbPb sample. ($150\mu b^{-1}$)	20
4.2	FSR parameter estimation from MC.	21
4.3	FSR parameter estimation from like-sign subtracted data.	22
4.4	Mass fits, with background constrained from like-sign dimuon spectrum.	25
4.5	Mass fit, with background constrained from the track-rotated like-sign dimuon spectrum shown in magenta ($\mu > 4.0, 150\mu b^{-1}$).	27
4.6	Mass fit, with background constrained from the track-rotated unlike-sign dimuon spectrum shown in magenta points. The magenta curve is normalized to like-sign pairs yield.	28
4.7	Compare like-sign, track rotation, and unlike-sign pairs	29

4.8	Mass fits to the pp data ($231nb^{-1}$) with error function. Figs 4.8(a), 4.8(b): signal shape parameters are left floating; Figs 4.8(c), 4.8(d): signal shape parameters are fixed to the PbPb results.	30
4.9	Mass fits to the pp data ($231nb^{-1}$), using like-sign information. Figs 4.9(a), 4.9(b): signal shape parameters are left floating; Figs 4.9(c), 4.9(d): signal shape parameters are fixed to the PbPb results.	31
5.1	Examples of tag-probe pair mass fits used to extract the trigger efficiency for data and MC.	38
5.2	Trigger efficiency measurements with tag and probe, and dependencies on probe muon and pseudo-rapidity and event centrality. The efficiencies measured in the full samples are represented as open symbols and the corresponding numerical values are displayed for data and simulation.	39
5.3	Examples of tag-probe pair mass fits for the muon identification efficiency in MC and data.	41
5.4	Muon identification efficiency measurements with tag and probe, and dependencies on probe muon and pseudo-rapidity and event centrality. The efficiencies measured in the full samples are represented as open symbols and the corresponding numerical values are displayed for data and simulation.	42
5.5	Examples of tag-probe pair mass fits for the inner tracking efficiency.	43
5.6	Tracking efficiency measurements with tag and probe, and dependencies on probe muon and pseudo-rapidity and event centrality. The efficiencies measured in the full samples are represented as open symbols and the corresponding numerical values are displayed for data and simulation.	44
6.1	$\Upsilon(3S)$ significance, estimated via likelihood ratio, by allowing and disallowing $\Upsilon(3S)$ p.d.f. in two fits.	47
6.2	Upper limit results for R_3 in PbPb using the Feldman-Cousins method. Shown is a p -value scan using 1000 pseudo experiments for each scanned point. The 95% C.L. upper limit corresponds to the point where the observed CLs crosses the 0.05 horizontal/red line.	50
6.3	95% interval on χ_3 with Feldman Cousins technique after including systematic uncertainties.	50
6.4	95% interval on χ_3 with profile likelihood calculator not including systematic uncertainties.	51
6.5	p -value scan for $R_{AA}(\Upsilon(3S))$ using the Feldman-Cousins technique.	53

6.6	A thousand pseudo-experiments for each of the ten points scanned. H_{sb} ; red curve, H_b blue curve and black line is the test statistic. As we increase our parameter of interest it is easier to differentiate between the two hypotheses and the area under the red curve becomes smaller than the area under the blue curve.	54
6.7	Profiled likelihood ratio. It shows the confidence interval at 95% confidence level.	55
6.8	p -value scan for $R_{AA}(\Upsilon(3S))$ using the Feldman-Cousins technique at 68 % confidence level.	56
6.9	Upper limit results using the Feldman-Cousins method on R_3 in PbPb, evaluated for the different centrality bins. (<i>Note: being updated</i>)	58
6.10	CLs and Bayesian cross checks for the centrality integrated bin, using uniform prior. Figs 6.10(a), 6.10(b): p -value Scan with different test statistics using 1000 pseudo experiments at each point; Figs 6.10(c), 6.10(d): Two different Bayesian approaches: Numerical calculation and Markov Chain Monte Carlo. (<i>Note: being updated</i>)	59
6.11	Bayesian results for 40-50% centrality bin. Figures 6.11(a), 6.11(b): Bayesian Numeric Calculator and Montecarlo Markov Chain. (<i>Note: being updated</i>)	60
7.1	Nominal mass fits, performed separately to the PbPb($150\mu b^{-1}$) and $pp(231nb^{-1})$ full datasets.	63
7.2	PbPb fit model variations ($150\mu b^{-1}$).	66
7.3	Centrality dependence of the PbPb single ratio, for $\mu > 4.0$. ($150\mu b^{-1}$).	69
7.4	Centrality dependence of the double ratios χ_{23} and χ_2 ; the PbPb statistical and systematic uncertainties are included; the graphs are normalized by the corresponding pp single-ratio central values; pp uncertainties are represented by gray box at unity, and are excluded from the data points as they do not affect point-to-point trend comparison. ($150\mu b^{-1}$).	71
7.5	Replace the negative error bars in Fig. 7.4 with Feldman-Cousins limits.	72
7.6	Simultaneous fit to the PbPb($150\mu b^{-1}$) and $pp(231nb^{-1})$ datasets, for $\mu > 4.0$	76
7.7	Mass fits in ranges of dimuon rapidity.	78
7.8	Mass fits in ranges of dimuon momentum.	79
7.9	Rapidity and dependences of the double ratios.	80
7.10	Mass projections of the fit overlaid with the same fit under the assumption of the null hypothesis show in the dashed green curve, used in the estimation of the significance.	81

7.11 Mass projections of the fit overlaid with the same fit under the assumption of the null hypothesis show in the dashed green curve, used in the estimation of the significance; the fit is performed in a restricted mass range, as to account for the systematic and statistical uncertainties, as described in the text.	82
7.12 Distributions of χ_{23} from pseudo-experiments generated under the hypothesis of no suppression. The arrow indicates the χ_{23} value that would correspond to 3σ significance.	85
7.13 Distributions of χ_2 from pseudo-experiments generated under the hypothesis of no suppression. The arrow indicates the χ_2 value that would correspond to 4σ significance (systematic included).	86
7.14 Mass projections of the fit overlaid with the same fit under the assumption of the null hypothesis show in the dashed green curve, used in the estimation of the significance. Null hypothesis: $\Upsilon(1S)R_{AA} = 1, \Upsilon(2S)R_{AA} = 1, \Upsilon(3S)R_{AA} = 1$	87
7.15 Mass projections of the fit overlaid with the same fit under the assumption of the null hypothesis show in the dashed green curve, used in the estimation of the significance. Null hypothesis: $\Upsilon(2S)R_{AA} = 1, \Upsilon(3S)R_{AA} = 1$	88
7.16 Mass projections of the fit overlaid with the same fit under the assumption of the null hypothesis show in the dashed green curve, used in the estimation of the significance. Null hypothesis: $\Upsilon(1S)R_{AA} = 1$	89
7.17 Mass projections of the fit overlaid with the same fit under the assumption of the null hypothesis show in the dashed green curve, used in the estimation of the significance. Null hypothesis: $\Upsilon(1S)R_{AA} = 1$. (<i>centrality</i> < 10% cut is used for the PbPbsample.)	90
7.18 Illustration of the excited to ground states relative Υ suppression in PbPb compared to pp , and comparison of the effect observed using the 2010 (<i>left</i>) and 2011 (<i>right</i>) PbPb datasets. The fit to the PbPb data, shown by the continuous line, is overlaid with the result of the pp fit, represented by the dashed line (shown on top of a common PbPb background shape, for comparison). For a better comparison, the background shape, background yield, mass peak width, mass peak tail shape and the $\Upsilon(1S)$ yields in the red line are fixed to the PbPb fit, while the $\Upsilon(2S)/\Upsilon(1S)$ and $\Upsilon(3S)/\Upsilon(1S)$ ratios are fixed to the pp fit values. These plots are provided for illustration, and do not reflect the analysis details.	94

7.19 Dimuon invariant-mass distribution from the PbPbdata, with the fit results shown as the solid (data + background) and dot-dashed (background-only) lines. The dashed curve illustrates the corresponding signals in pp data, scaled by the R_{AA} values. The same reconstruction algorithm and analysis criteria are applied to the PbPband pp datasets, including a transverse momentum requirement on single muons of > 4 95

List of Tables

4.1	Final state radiation and resolution parameter values.	22
5.1	Tag and probe efficiency measurements in PbPbdata and simulation; an acceptance cut $\mu > 4.0$ on the probe muons is applied; values are in percent, and errors are statistical only.	45
5.2	Tag and probe efficiency measurements in pp data and simulation; an acceptance cut $\mu > 4.0$ on the probe muons is applied; values are in percent, and errors are statistical only; results from [?].	45
6.1	$R_{AA}(\Upsilon(3S))$ upper limits. (<i>Note: being updated</i>)	56
6.2	Single-ratio upper limits. (<i>Note: being updated</i>)	58
6.3	Single-ratio credible intervals: Bayesian cross checks. (<i>Note: being updated</i>)	58
7.1	Summary of single-ratio results, for the PbPb dataset.	67
7.2	Summary of single-ratio results for the 2.76 TeV dataset.	68
7.3	Double-ratio results.	91
7.4	R_{AA} significance computed with profile likelihood ratio	92

Chapter 1

Introduction

Bayesians are like Vegans, at some point they become impractical.

Meetup in the Silicon Valley

If a deconfined medium is formed in high-energy heavy-ion collisions, one of its most striking expected characteristics is the suppression of quarkonium states. This takes place as the force between the constituents of the quarkonium state, a heavy quark and its antiquark, is weakened by the color screening produced by the surrounding light quarks and gluons. The suppression is predicted to occur above a critical temperature of the medium, and sequentially, in the order of the $Q\bar{Q}$ binding energy. Since the $\Upsilon(1S)$ is the most tightly bound state among all quarkonia, it is expected to be the one with the highest dissociation temperature. Such a suppression pattern is expected to further depend on complications arising from additional phenomena sometimes referred to as *hot* and *cold* nuclear matter effects. This work presented here aims at studying in detail the bottomonium family of states in ultra-relativistic heavy-ion collisions. Given the momentum

resolution attained, and the capability of the trigger system, CMS is unrivaled in the analysis of the Υ family in the three environments studied (pp, pPb and PbPb)

1.1 Heavy Ion Physics

The study of the fundamental theory of the strong interaction — Quantum Chromodynamics (QCD) — in extreme conditions of temperature, density and parton momentum fraction (low- x) has attracted an increasing experimental and theoretical interest during the last 20 years. Indeed, QCD is not only a quantum field theory with an extremely rich dynamical content — such as asymptotic freedom, infrared slavery, (approximate) chiral symmetry, non-trivial vacuum topology, strong CP violation problem, $U_A(1)$ axial-vector anomaly, colour superconductivity, ... — but also the only sector of the Standard Model (SM) whose full *collective* behaviour — phase diagram, phase transitions, thermalisation of fundamental fields — is accessible to scrutiny in the laboratory. The study of the many-body dynamics of high-density QCD covers a vast range of fundamental physics problems (Fig. 1.1).

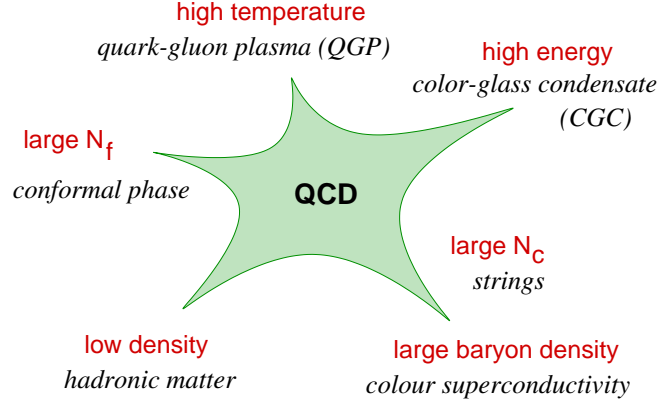


Figure 1.1: Many-body dynamics of QCD in different physics limits.

Deconfinement and chiral symmetry restoration

Lattice QCD calculations predict a new form of matter at energy densities (well) above a critical value — $\epsilon_c = (6 \pm 2)T_c^4 \approx 1 \text{ GeV/fm}^3$ (Fig. 1.2), where $T_c \approx 150\text{--}190 \text{ MeV}$ is the critical temperature — consisting of an extended volume of deconfined and current-mass quarks and gluons: the Quark-Gluon Plasma (QGP).

The vanishing of the chiral condensate at T_c and the sudden liberation of quark and gluon degrees of freedom are clearly visible in Fig. 1.2. The scrutiny of this new state of matter — equation-of-state (EoS), order of the phase transition, transport properties, etc. — promises to shed light on basic aspects of the strong interaction such as the nature of confinement, the mechanism of mass generation (chiral symmetry breaking, structure of the QCD vacuum) and hadroniza-

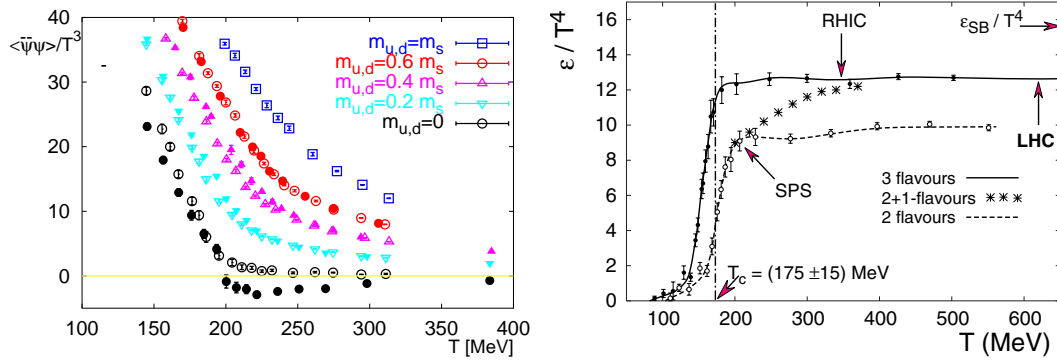


Figure 1.2: Left: The light quark chiral condensate versus the temperature computed in lattice QCD with various number of flavours and values of the u, d, s quark masses. Right: The energy density in QCD with 0, 2 and 3 degenerate quark flavours as well as with two light and one heavier (strange) quarks. The horizontal arrow shows the value of the Stefan-Boltzmann limit for an ideal quark-gluon gas

tion, which still evade a thorough theoretical description due to their highly non-perturbative nature.

In order to calculate physical observables from first principles in QCD it is not enough to know its Lagrangian. It is also necessary and important to know the true structure of its ground state. It is just the response of the true QCD vacuum which substantially modifies all the QCD Greens functions from their free counterparts.

Parton structure and evolution at small- x

HERA results indicate that when probed at high energies, hadrons consist of a very dense system of gluons with small (Bjorken) momentum $x = p_{\text{parton}}/p_{\text{hadron}}$.

At low x , the probability to emit an extra gluon is large, proportional to $\alpha_s \ln(1/x)$, and gluon-gluon fusion processes will eventually dominate the parton evolution in the hadronic wavefunctions. At high virtualities Q^2 and moderately low x , such evolution is described by linear DGLAP or BFKL equations, suitable for a dilute parton regime. At $x \lesssim 10^{-2}$, and for Q values below an energy-dependent saturation momentum Q_s , hadrons are however more appropriately described as dense, saturated parton systems in the context of the “Colour-Glass Condensate” (CGC) effective theory with the corresponding non-linear JIMWLK evolution equations (Fig. 1.3). Low- x gluons in nuclei overlap and, so, saturation effects are expected to set in earlier for ultrarelativistic heavy nuclei (for which $Q_s^2 \propto A^{1/3}$, with A the number of nucleons) than for free nucleons.

1.2 Quarkonia

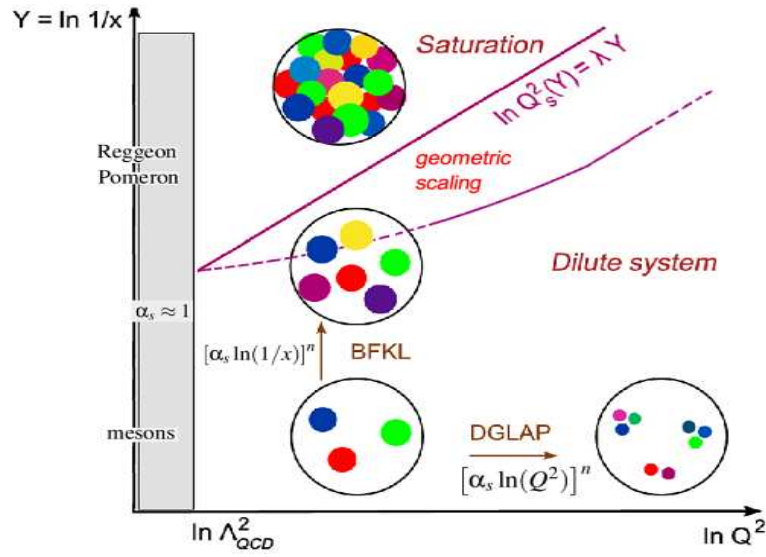


Figure 1.3: QCD phase diagram in the $1/x, Q^2$ plane (each circle represents a parton with transverse area $\sim 1/Q^2$ and fraction x of the hadron momentum). The different evolution regimes (DGLAP, BFKL, saturation) are indicated, as well as the saturation scale and geometric scaling curves between the dense and dilute domains

Chapter 2

Measurments

The LHC allows for the first detailed studies of the bottomonium family of states in ultra-relativistic heavy-ion collisions. Given the momentum resolution attained, and the capability of the trigger system, CMS is well positioned to lead these studies. The measurement of bottomonium production and suppression is presented, based on the dataset collected by the CMS experiment during the 2011 PbPb collision run at $\sqrt{s_{NN}} = 2.76$.

If a deconfined medium is formed in high-energy heavy-ion collisions, one of its most striking expected characteristics is the suppression of quarkonium states [?]. This takes place as the force between the constituents of the quarkonium state, a heavy quark and its antiquark, is weakened by the color screening produced by the surrounding light quarks and gluons. The suppression is predicted to occur above a critical temperature of the medium, and sequentially, in the order of the $Q\bar{Q}$ binding energy. Since the $\Upsilon(1S)$ is the most tightly bound state among all

quarkonia, it is expected to be the one with the highest dissociation temperature. Such a suppression pattern is expected to further depend on complications arising from additional phenomena sometimes referred to as *hot* and *cold* nuclear matter effects [?, ?]. The study of charmonium (J/ψ , ψ' , χ_c) and bottomonium ($\Upsilon(1S)$, $\Upsilon(2S)$, $\Upsilon(3S)$, χ_b) production at the unprecedented medium created at the LHC is accordingly much awaited. In this note, the measurements of the production and suppression of the $\Upsilon(1S)$, $\Upsilon(2S)$, and $\Upsilon(3S)$ states are performed.

The production of $\Upsilon(nS)$ states is studied by comparing their production rates in PbPb and pp collision data, taken at the same collision energy of $\sqrt{s_{NN}} = 2.76$. In particular, the yield of the higher-mass states is measured relative to the ground state. In this way, we explore the double ratios – $\Upsilon(2S, 3S)$ *vs* $\Upsilon(1S)$ and PbPb *vs* pp – which allows a self-calibrating measurement. Several effects associated to selection, acceptance, and reconstruction mostly cancel, and only remaining factors need to be accounted for, as corrections to the fitted ratio of raw signal yields.

Based on the dataset collected during the first LHC PbPb run, at $\sqrt{s_{NN}} = 2.76$, in 2010, and in the special run at the same energy in early 2011, CMS has published first results on upsilon production and suppression in PbPb collisions. These included the first evidence for suppression of the excited Υ states relative to the ground state, at the 2.4σ level [?, ?]. Suppression of the $\Upsilon(1S)$ state,

relative to collisions at the same energy, has also been measured [?, ?]. These two measurements were found to be consistent with suppression of only the excited states, which result in reduced feeddown from excited to ground states. These main results may be summarized as follows:

$$\begin{aligned}
\Upsilon(2S + 3S)/\Upsilon(1S)|_{\text{PbPb}} &= 0.24^{+0.13}_{-0.12} \pm 0.02, \\
\Upsilon(2S + 3S)/\Upsilon(1S)|_{pp} &= 0.78^{+0.16}_{-0.14} \pm 0.02, \\
(\chi \equiv) \frac{\Upsilon(2S + 3S)/\Upsilon(1S)|_{\text{PbPb}}}{\Upsilon(2S + 3S)/\Upsilon(1S)|_{pp}} &= 0.31^{+0.19}_{-0.15} \pm 0.03, \\
(R_{AA} \equiv) \frac{\Upsilon(1S)|_{\text{PbPb}; 0-20\%}}{\Upsilon(1S)|_{pp}} &= 0.681 \pm 0.143 \pm 0.119.
\end{aligned}$$

In the 2011 PbPb run, CMS collected a dataset approximately 20 times larger than that gathered in 2010. These data will be scrutinized, in order to extract further novel and precision results, during the few years ensuing datataking. In what follows, the corresponding analysis of upsilon suppression is detailed.

Chapter 3

Datasets

3.0.1 PbPb dimuon trigger and skim

A primary dataset (/HIDiMuon/HIRun2011-PromptReco-v1/RECO) based on all events selected by the muon trigger has been used for this analysis. The RAW files and the prompt reconstruction files are stored at T1_FR_CCIN2P3. At the Tier-1, they were skimmed for events with two global muons that form a pair with an invariant mass of more than 2(/HIDiMuon/tdahms-Onia2MuMu_Skim-v3-*/USER). All charge combinations have been considered in the pairing. In addition to a muon trigger firing in the event a coincidence with the minimum bias trigger was required. This minimum bias trigger was defined by the logical or of the following three triggers, which were unprescaled during the run:

- A bunch crossing signal sent by the BPTX (BptxAND) and, two coincident HF towers above a certain threshold (set in the firmware) on each side of the detector (HcalHfCoincPm) or at least one BSC segment (of the 16) giving a signal on each side of the detector (BscMinBiasThreshold 1):

L1_HcalHfCoincPmORBscMinBiasThresh1_BptxAND_instance1.

- BSCThreshold1 which requires at least one BSC hit on each side (out of the 32 channels): 'L1_NotBsc2_BscMinBiasOR'. 'NotBsc2' is always 'True' so it can be ignored.

- coincidence of two HF towers on each side of the detector: HFL1_HcalHfCoincidencePm.■

Signal candidates are required to have fired the trigger path HLT_HIL1DoubleMu0_HighQ.■

This trigger was unrescaled during the whole run. It is based solely on L1 decisions and requires the presence of two L1 muon objects with quality > 4, without any constraint on their momenta. Coincidence with the BPTX trigger is required. The trigger path has tighter quality requirements than the path HLT_HIL1DoubleMuOpen used in the 2010 PbPbrun, and than the path HLT_L1DoubleMu0 used in the 2011 *pp*2.76TeV run.

Furthermore, the default good event selection as in the 2010 analysis has been applied. This requires a veto on BSC halo triggers, a reconstructed primary vertex with two or more tracks, and the pixel cluster-length being compatible with the

primary vertex to reject PKAM events. An additional requirement to remove UPC (ultra-peripheral collisions) events was the offline HF coincidence, requiring at least 3 HF towers on each side of the interaction point with at least 3 energy deposited per tower.

In summary, the events used for this analysis are required to pass the following filters : the BSC halo filter, a reconstructed primary vertex made of at least two tracks, the pixel cluster-length compatibility with the vertex, the requirement of an off-line HF coincidence with at least 3 towers on each side of the interaction point in the HF with at least 3 GeV energy deposited per tower, and the HLT_HIL1DoubleMu0_HighQ muon trigger.

The CMSSW release 4_4_2_patch5 and the global tag GR_P_V27A were used during the skimming and analysis steps.

3.0.2 pp sample

The same *pps* sample as for the 2010 analysis has been used [?, ?, ?]. Signal candidates are required to have fired the trigger path HLT_L1DoubleMu0. The data have been re-reconstructed in the same CMSSW release as the 2011 PbPb data (4.4.2_patch5) with the global tag GR_R_44_V10: /AllPhysics2760/Nov2011_HI-SD_MuHI-276TeV_ppRereco/RECO.

3.0.3 Monte Carlo samples

$\Upsilon(1S)$ events were simulated in PYTHIA and embedded into HYDJET as for last year's analysis. For this $\Upsilon(1S)$ were generated with realistic and rapidity distributions in several bins of (0–3, 3–6, 6–9, 9–12, 12–15, 15–30, and > 30) to enhance the statistics at high :

/Hydjet_Bass_MinBias_2760GeV/davidlw-PyquenEvtGen_ulsMuMu_upsPt*-■

Summer11-STARHI44_V7-v1-GEN-SIM-RECO_v3-58956c214fa8e92cbba029d2c88707a9/USER■

Chapter 4

Fitting

The parameters of interest are extracted from the data samples via an extended unbinned maximum likelihood fit to the dimuon invariant-mass spectra. In this section, the fitter study is carried out for two selected p_T^μ cut, 3.5 and 4.0 . But the final results in Section ?? is given with the nominal 4.0 cut only. The baseline fitting model is improved relative to the publication using the 2010 dataset. We explored complementary approaches for background modeling (eg employing like-sign parameterizations, track rotation).

The baseline fitting model is inspired in that used in [?, ?]. Each of the $\Upsilon(nS)$ signals is modeled via a crystal-ball shape (CB), which consists of a Gaussian function with the low-side tail replaced with a power law describing final-state

radiation (FSR). The crystal-ball function is given by:

$$f(x; \alpha, n, \bar{x}, \sigma) = N \cdot \begin{cases} \exp(-\frac{(x-\bar{x})^2}{2\sigma^2}) & \text{for } \frac{x-\bar{x}}{\sigma} > -\alpha \\ A \cdot (B - \frac{x-\bar{x}}{\sigma})^{-n} & \text{for } \frac{x-\bar{x}}{\sigma} \leq -\alpha, \end{cases} \quad (4.1)$$

where

$$\begin{aligned} A &= \left(\frac{n}{|\alpha|} \right)^n \cdot \exp \left(-\frac{|\alpha|^2}{2} \right), \\ B &= \frac{n}{|\alpha|} - |\alpha|. \end{aligned}$$

The CB function is parameterized by four parameters – the mass mean \bar{x} and resolution σ , and the tail parameters α and n – which are constrained amongst the three signal peaks: the tail parameters are common; the resolution forced to scale with the resonance mass; the differences of the mass means are fixed to their PDG values.

In the previous iteration of the analysis [?], based on the 2010 dataset, the signal PDF shape parameters were fixed from MC simulation: $\alpha = 1.6$, $n = 2.3$, $\sigma_{1S} = 92$. In view of the larger dataset currently available, such constraints have been relaxed. Specifically, the following signal shape parameters are free in the fit: the $\Upsilon(1S)$ mass mean and resolution, the tail parameter α . Note that, given α and n are strongly correlated, the constraint $n = 2.3$ is kept in the fit.

The threshold applied for muon selection induces a sculpting of the mass background distribution, as described in Section ???. The background parameterization adopted corresponds to an exponential function (exp), multiplied by an error-function (erf), where the latter describes the induced kinematic shoulder and is defined as:

$$\text{erf}(x) = \frac{2}{\sqrt{\pi}} \int_0^x e^{-t^2} dt \quad (4.2)$$

The background model is thus described by three parameters: the exponential decay constant, and the turn-on mean and width. All background parameters are left free.

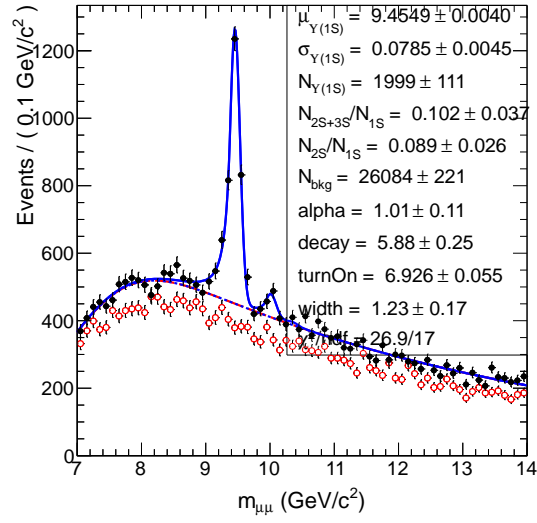
The nominal fit results to the PbPb data are shown in Fig. 4.1.

4.0.4 Signal model studies

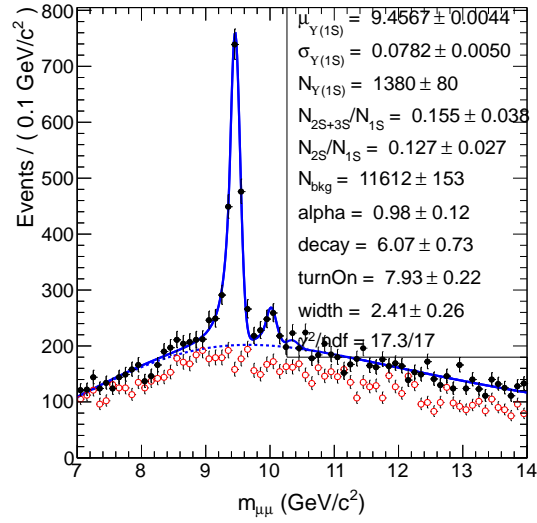
Final state radiation model

We first estimate the CB tail from Monte Carlo simulation of final state radiation. The MC sample is first split in multiple (about 50) sub-samples, of statistics comparable to data. These samples are fitted in turn, and the average parameter values are determined. This is shown in Fig. 4.2.

For estimating the CB tail from data, the fit is performed after subtracting the like-sign dimuon mass distribution. This procedure results in a mostly flat

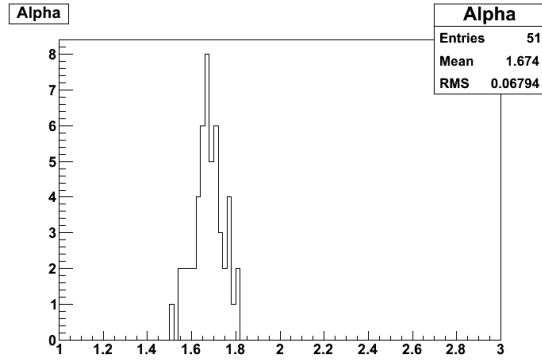


(a) $\mu > 3.5$

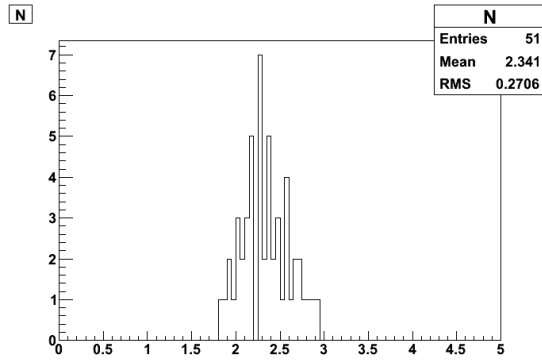


(b) $\mu > 4.0$

Figure 4.1: Fit to the dimuon invariant-mass distributions, for the PbPb sample. ($150\mu b^{-1}$)



(a) fixed: $\sigma = 92$, $n = 2.3$; float: α



(b) fixed: $\sigma = 92$, $\alpha = 1.674$; float: n

Figure 4.2: FSR parameter estimation from MC.

remaining background. In this way, the (binned) fit to the subtracted data is able to better constrain the background shape from the mass side-bands, allowing also a more reliable determination of the CB tail. Fit examples are shown in Fig. 4.3.

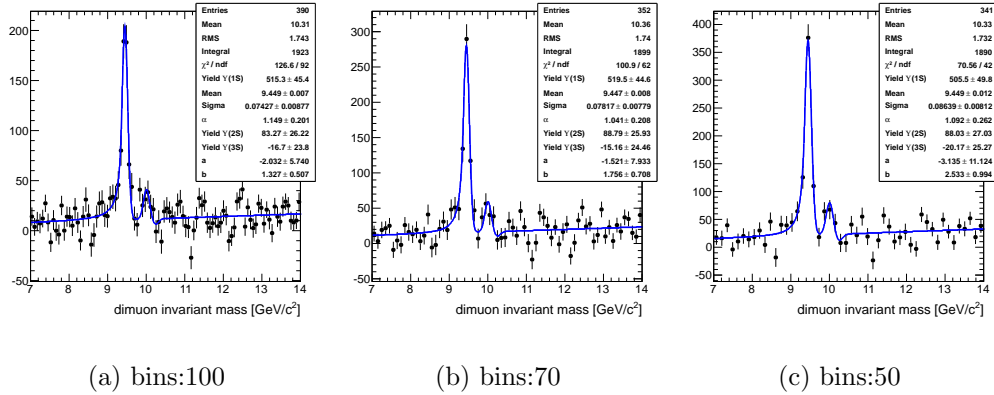


Figure 4.3: FSR parameter estimation from like-sign subtracted data.

Table 4.1 summarizes the CB tail parameter estimations achieved from simulation and data. It illustrates the level of variations that may be attained. In the nominal configuration, the α CB parameter is determined from the fit to the data.

Table 4.1: Final state radiation and resolution parameter values.

	α	n (fixed)	σ ()
Monte Carlo	1.67	2.3	90
$pp7$ TeV data	1.4 ± 0.1	2.3	62 ± 2
like-sign subtracted PbPbdata	1.0 ± 0.3	2.3	$73 - 87$
PbPbdata (nominal fit)	0.98 ± 0.2	2.3	78.2 ± 0.5
PbPband pp data (nominal simul. fit)	1.12 ± 0.13	2.3	79.4 ± 0.4

4.0.5 Background model studies

We explore alternative estimations and parameterizations of the background, with respect to the second order polynomial model used in [?, ?].

Like-sign dimuon spectrum

Here we carry out fits to the upsilon data, by constraining the background model utilizing information from the like-sign dimuon spectrum. The like-sign dimuon combinations contain no signal component, and provide a useful handle to estimate the combinatorial background shape in the mass region under the signal peaks. The like-sign spectrum is not expected to match *exactly*, in shape and normalization, the combinatorial opposite-side spectrum: different, small contributions may arise from Drell-Yan and open flavor sources. This residual component is expected to be smooth and non-peaking, and is accommodated by allowing an extra polynomial component in the fit the (oppositely charged dimuon) data.

The like-sign dimuon mass distribution is employed to define a PDF component, in the following two ways:

- **Like-sign dataset smoothing.** We use the RooFit implementation via the class RooKeysPdf [?], which implements a one-dimensional kernel estimation PDF which models (smoothens) the distribution as a superposition

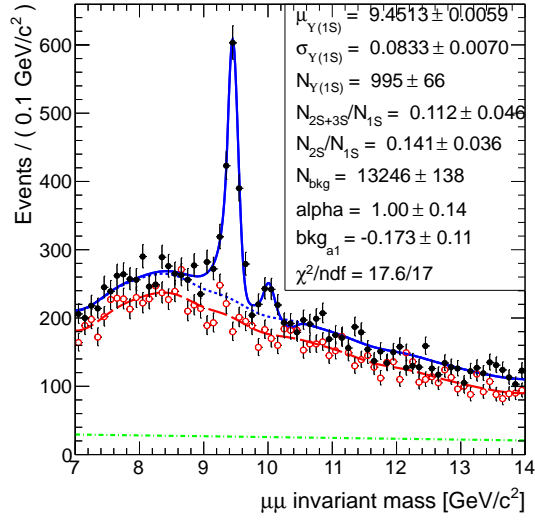
of Gaussian kernels, one for each data point, each contributing $1/N$ to the total integral of the PDF.

- **Like-sign parameterized fit.** We fit the like-sign distribution utilizing an $\text{Erf} \times \text{Exp}$ model. The high-mass spectrum is well described by an exponential, describing random track combinations. To describe the acceptance turn-on shape induced by the single muon kinematic threshold, the exponential is multiplied by an error function. Tested variations of the turn-on function parameters gave negligible deviations of the extracted yields.

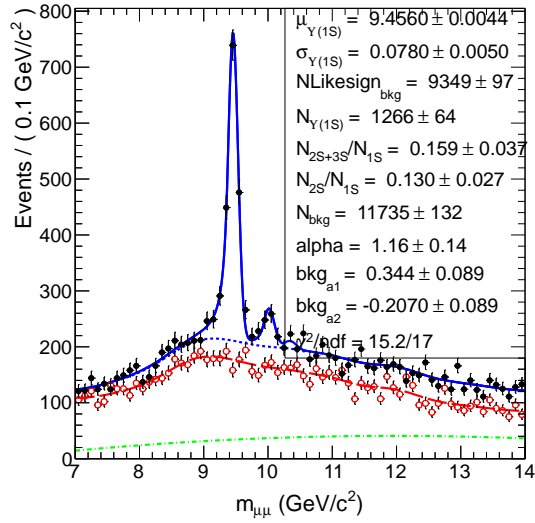
The shape of the like-sign distribution matches well that of the mass sidebands in the opposite-sign sample. The fit to the opposite-sign signal sample is performed employing a linear combination of the like-sign extracted PDF, along with an extra polynomial component. The latter is included in order to allow for potential discrepancies that might arise between the like-sign and opposite-sign mass spectra. The fit results are displayed in Fig. 4.4 and demonstrate a good description of the data.

Track-rotation method

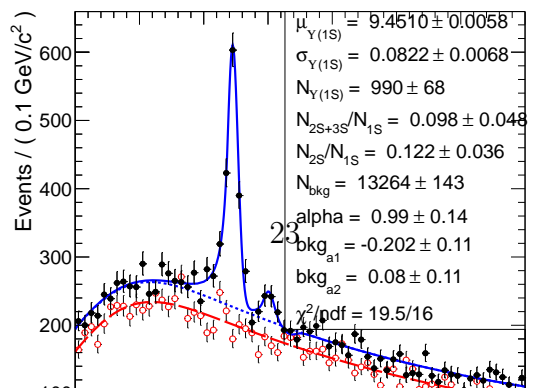
We explore an independent method to estimate the combinatorial background. This is normally referred to as “track-rotation method” and consists of the following steps: (i) all like-sign muon pairs (or the unlike-sign muon pairs) in the event



(a) $\mu > 3.5$, rookeyspdf, $70\mu b^{-1}$



(b) $\mu > 4.0$, rookeyspdf, $150\mu b^{-1}$



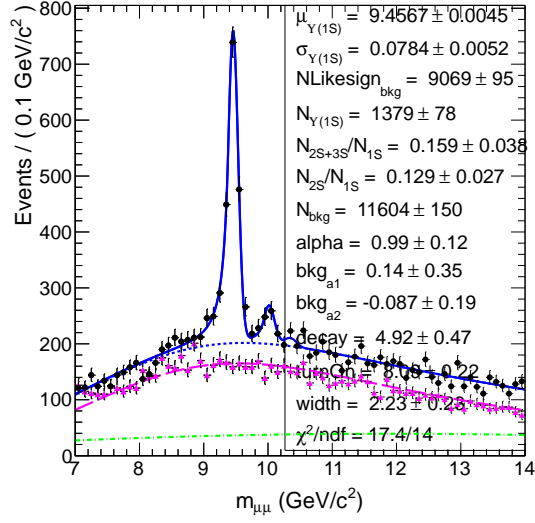
are formed, (ii) for each pair, one of the muons is randomly selected, and (iii) its ϕ coordinate is rotated by π . In this way we obtain an uncorrelated sample of tracks, extracted directly from the data and thus matching the data kinematics, from which the combinatorial mass distribution can be estimated.

Having extracted the combinatorial background PDF, the same fitting strategy as described in Sec. 4.0.5 for the like-sign case is employed when fitting the oppositely charged dimuon data. The track rotation PDF is normalized to like-sign yield. The results are shown in Fig. 4.5 for like-sign, in Fig. 4.6 for unlikesign. They display a good description of the data. A comparison of like-sign pairs shape, track rotation pairs shape, and unlike-sign pairs shape is shown in Fig. 4.7.

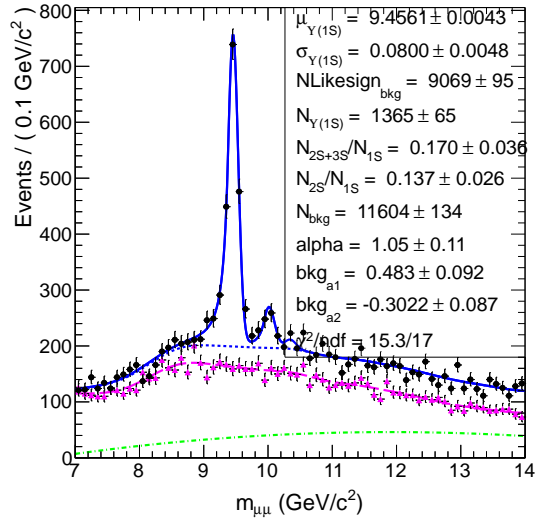
4.0.6 Fits to the pp data

The $pp2.76$ TeV dataset is the same as employed in the previous measurement [?]. The same background fitting model as employed therein is adopted as nominal for the pp case: second order polynomial.

The same fitting model as devised for the PbPbdataset is applied to the pp dataset as well, to probe stability. Fit results are shown in Fig. 4.8 for the nominal background model (error function times exponential), and in Fig. 4.9 for fits utilizing like-sign information. The results are displayed for the $\mu > 3.5$ and $\mu > 4.0$ selections, and for the cases where the signal shape parameters are left

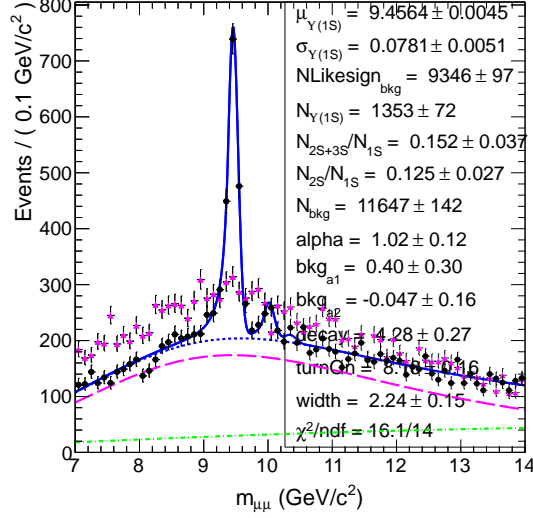


(a) erf*exp + pol.2

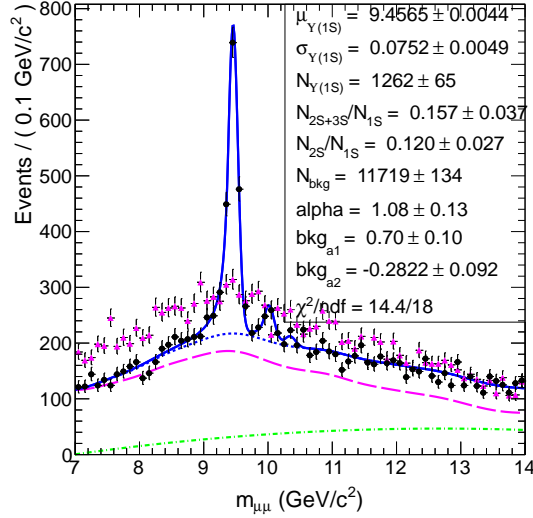


(b) keysPdf + pol.2

Figure 4.5: Mass fit, with background constrained from the track-rotated like-sign dimuon spectrum shown in magenta ($\mu > 4.0, 150\mu b^{-1}$).



(a) $\text{erf}^* \text{exp} + \text{pol.2}$



(b) $\text{keysPdf} + \text{pol.2}$

Figure 4.6: Mass fit, with background constrained from the track-rotated unlike-sign dimuon spectrum shown in magenta points. The magenta curve is normalized to like-sign pairs yield.

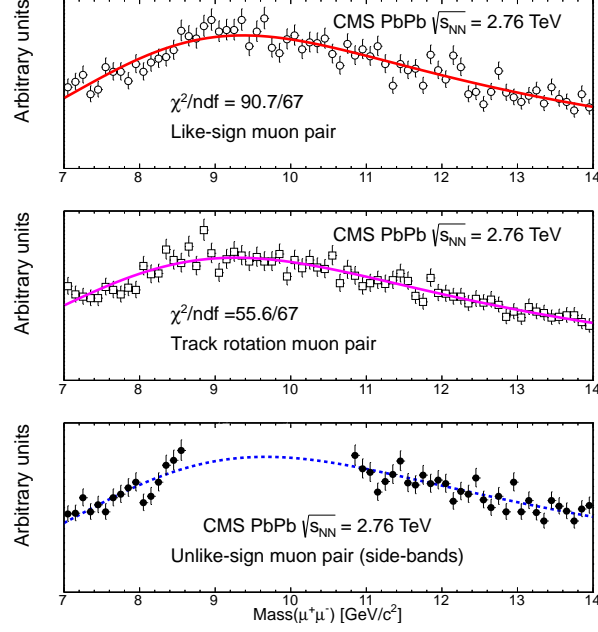
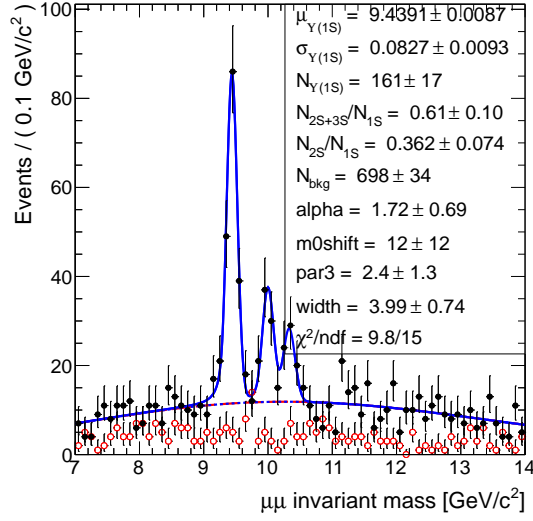
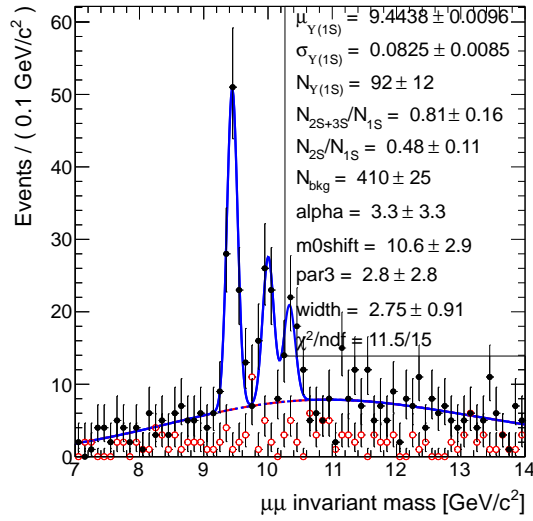


Figure 4.7: Compare like-sign, track rotation, and unlike-sign pairs

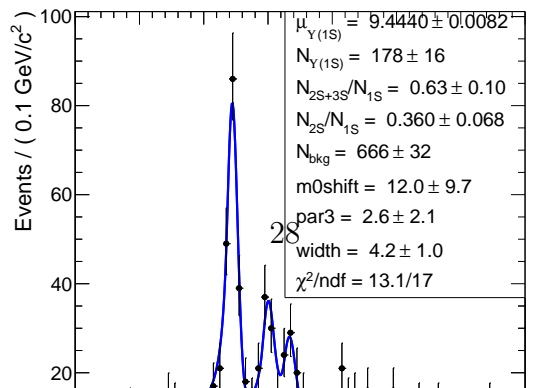
floating and are fixed to the PbPb results. Despite the excessive number of parameters of the background model, when applied to the limited-statistics pp dataset, the fit results show a fair stability.

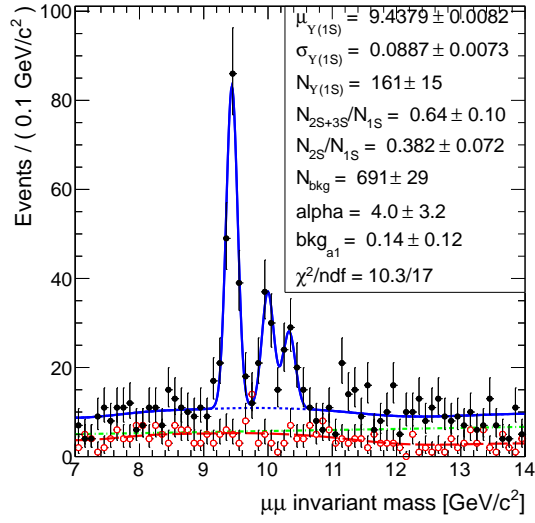


(a) $\mu > 3.5$

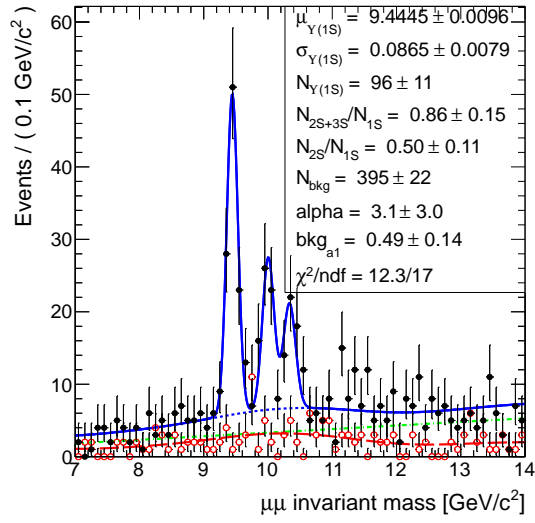


(b) $\mu > 4.0$

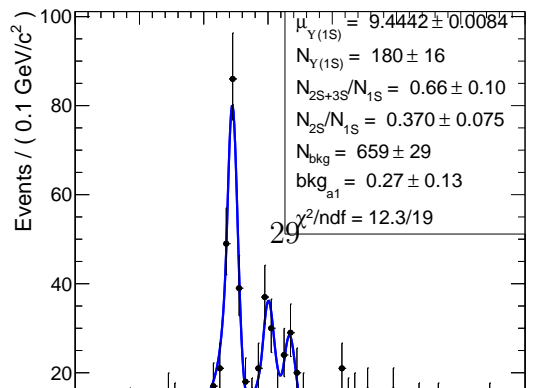




(a) $\mu > 3.5$



(b) $\mu > 4.0$



Chapter 5

Efficiency

We explore the data-driven tag and probe (T&P) method to estimate single-muon trigger, identification, and tracking efficiencies. A comparison of the results obtained by applying the technique to both data and MC simulation allows to estimate related systematic uncertainties.

The procedure is identical to that used in the previous analysis iteration, based in the 2010 PbPbdataset, documented in Ref. [?]. The T&P analysis is done using the official tag and probe framework, as employed for example in Ref. [?, ?]. The J/ψ signal resonance is used to differentiate signal from background. Two tag-probe invariant mass distributions are formed, in the vicinity of the J/ψ nominal mass, according to whether the probe passes or fails the criteria for which the efficiency is being measured. The two mass distributions are then fit simultaneously, and the efficiency ε (and its uncertainty) is extracted as a common parameter in

the fit,

$$N_{\text{pass}} = \varepsilon \times N_{\text{probes}} , \quad (5.1)$$

$$N_{\text{fail}} = (1 - \varepsilon) \times N_{\text{probes}} ,$$

where N_{probes} , N_{pass} , and N_{fail} are the number of all probes, passing probes, and failing probes, respectively.

Some challenges arise in measuring the tracking efficiency because in heavy ions fake and tracking efficiency can be “correlated” due to the high multiplicity, one can have a fake match in events in which one has removed the true match. Yet another problem is that measuring the matching efficiency between a standalone muon and an inner track (necessary to promote a standalone muon to a global muon) is not straightforward in heavy ions [?]. Furthermore, to fit failing tag and probe pairs becomes challenging due to the poor resolution of the standalone (STA) muons. In general, we will compare the efficiency estimations found with T&P in Monte Carlo simulation and data as a cross check of the Monte Carlo based efficiency corrections.

Tags are selected as high quality, global muons, which are matched to the single muon trigger path `HLT_HIL1SingleMu0_HighQ`, that also pass the offline muon selection used in the data analysis. These tag muons are combined with

probe muons to form tag-probe pairs. The probe muon selection depends on the efficiency being measured. A condition is applied to the probes which are split into the passing and failing probe categories. It is the efficiency of this condition relative to all probes that is measured with T&P. We have used the following three probe categories to measure the inner-track reconstruction, muon reconstruction and identification, and muon trigger efficiencies:

- inner-track reconstruction efficiency (including inner to outer track matching, and track quality criteria):
 - probe: a standalone muon (the four-momentum information is taken from the standalone part exclusively)
 - passing probe: probe that is also a global muon passing the quality cuts
- global muon reconstruction and identification efficiency (relative to tracker muon)
 - probe: tracker muon
 - passing probe: probe that can be matched to a global muon and that fulfills the analysis muon selection criteria
- trigger efficiency:

- probe: (global) muon that satisfies the offline analysis selection criteria
- passing probe: probe that can be matched to (one leg of) HLT_HIL1DoubleMu0_HighQ trigger path.

In order to attempt a reduction of the background level, further selection criteria have been tried. A requirement on the dimuon > 6.5 is applied as well as a single muon > 4.0 . In all cases, identical selection criteria are applied to both data and simulation: this is necessary for yielding reliable systematic estimates based on data-MC efficiency results comparison.

The efficiency in simulation is measured using T&P on a prompt J/ψ sample. The MC sample is weighted for the centrality dependence (which scales with N_{coll}) and for the relative weights between the different bins used in the sample production. While the T&P framework allows for weighted samples, the uncertainty estimates using the current version of RooFit for weighted datasets is not accurate. However, employing large MC statistics, we will take the size of the corresponding errors to be negligible.

The estimation of the systematic uncertainty will be assigned by comparing results between data and simulation. We also note that only results above the single-muon of 4.0 are within the acceptance used in the analysis. This tends to reach the muon efficiency plateau, and is less affected by systematics related to the detailed description of the efficiency turn-on.

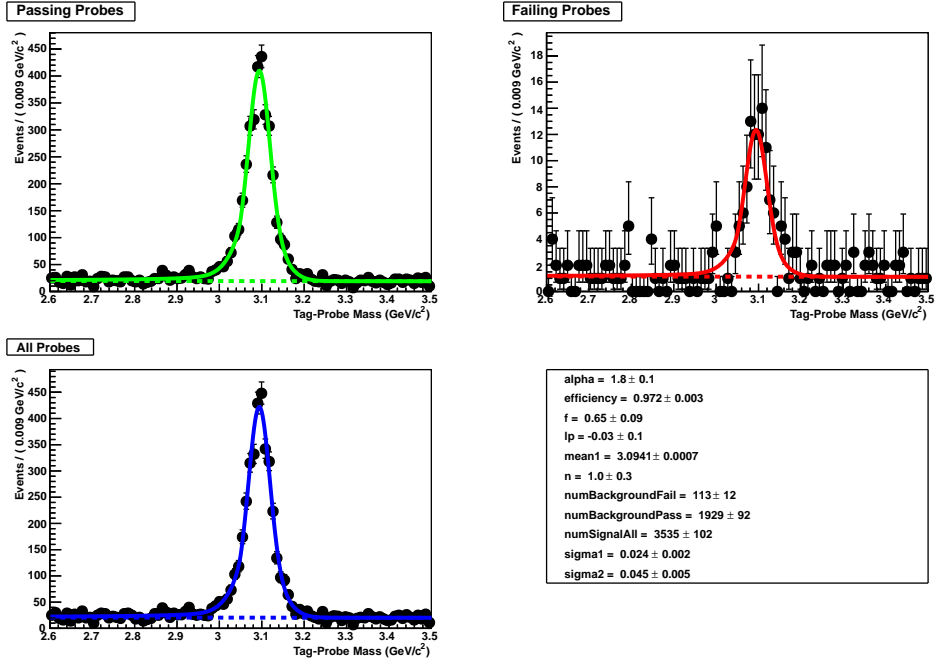
Trigger efficiency

The trigger efficiency is, in general, the easiest one to fit for, given the cleaner probe sample. The signal shape is describe by a Crystal Ball plus a Gaussian. The addition of the Gaussian is motivated to describe varying detector resolution. The parameters in the Crystal Ball as well as the width of the Gaussian are free parameters of the fit. The background is described by an exponential function.

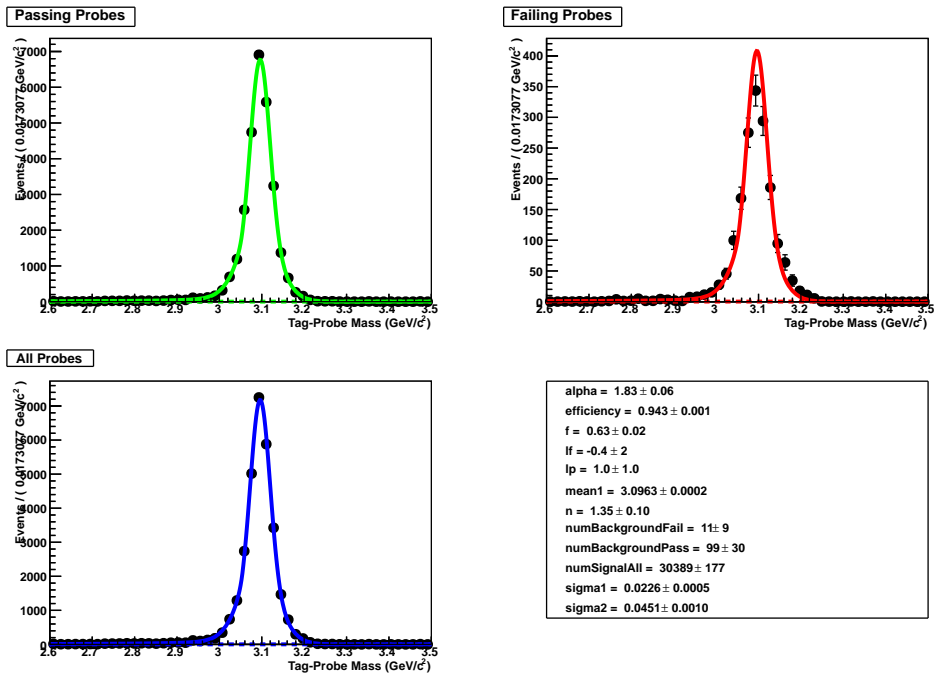
Figure 5.1 shows fits to the passing and failing samples of T&P pairs for the trigger efficiency measurement, using the integrated data and MC samples. Figure 5.2 shows the trigger efficiency measured as a function of probe and pseudo-rapidity. Also shown is the trigger efficiency as function of centrality which, as expected, shows no significant dependence. A reasonable agreement between data and simulation is obtained especially in the most peripheral bins.

Muon identification efficiency

We fit simultaneously the passing and failing tag-probe pairs mass distribution using a Crystal Ball function and (when needed to account for different resolutions) a Gaussian. A first order polynomial is used to describe the background. For the MC case, a Crystal Ball and an exponential describe the signal and background shapes.

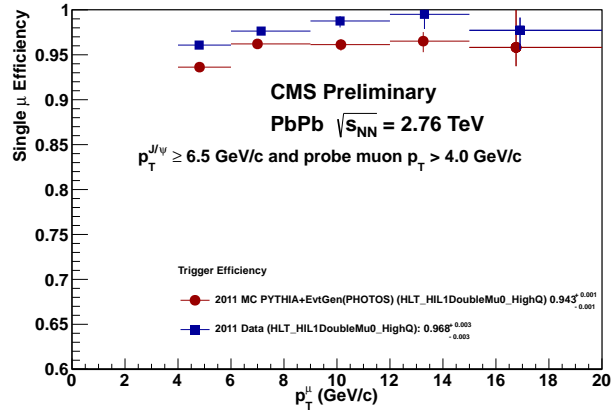


(a) Data

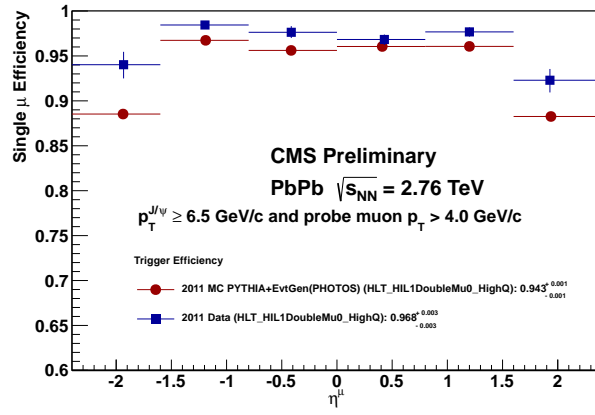


(b) Monte Carlo

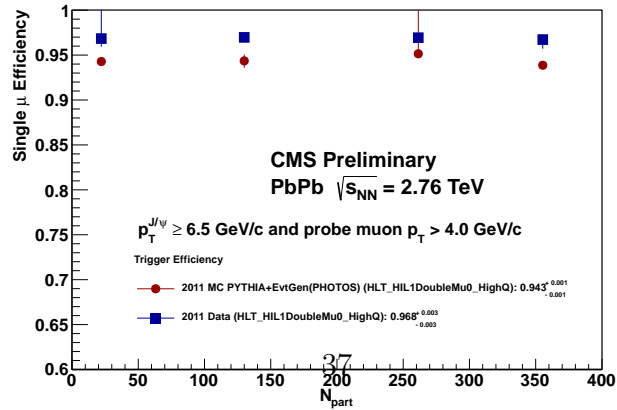
Figure 5.1: Examples of tag-probe pair mass fits used to extract the trigger efficiency for data and MC.



(a) Trigger efficiency dependence on muon p_T .



(b) Trigger efficiency dependence on muon η .



(c) Trigger efficiency dependence on event centrality.

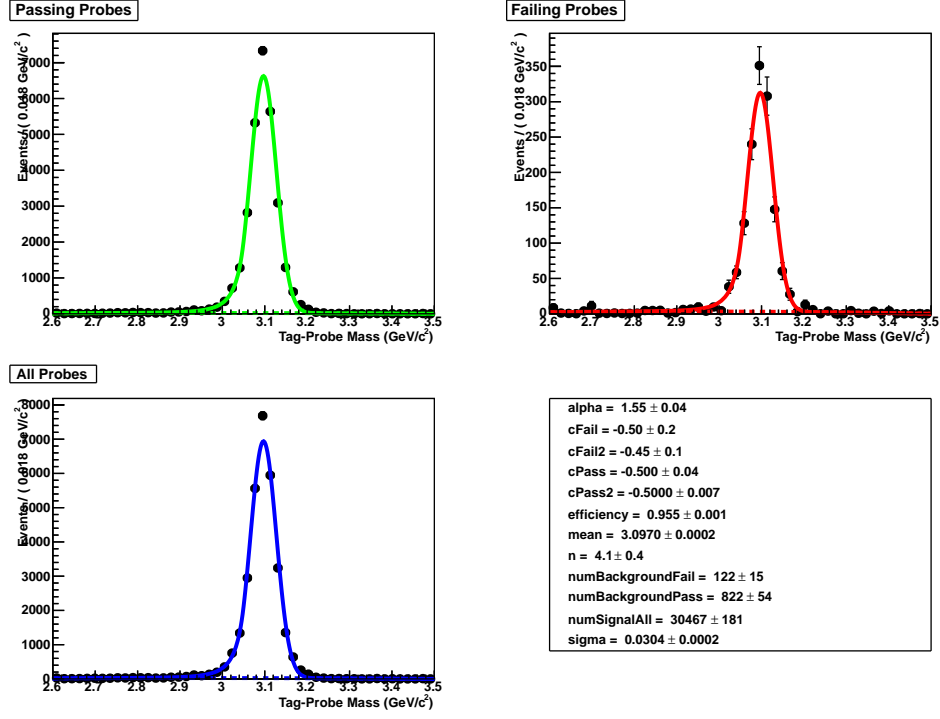
T&P mass fits for the muon identification efficiency are shown in Fig. 5.3, for the integrated data and MC samples. These illustrate the considerably high level of background involved, in the heavy-ion environment. Figure 5.4 shows the muon identification efficiency measured as a function of probe and pseudo-rapidity, and event centrality. A good agreement between data and simulation is observed.

Tracking efficiency

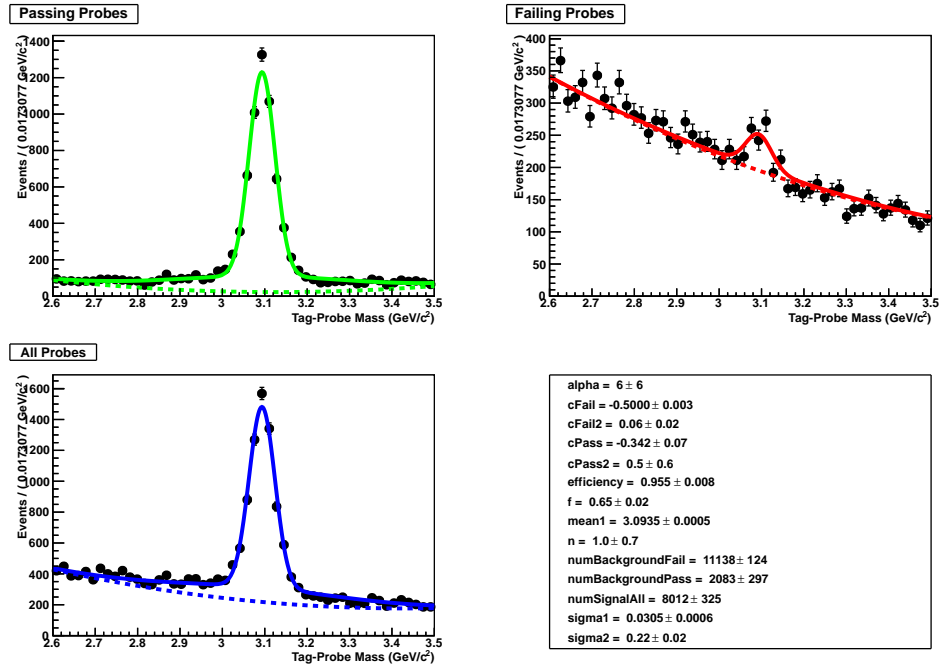
The fits for the tracking efficiency are challenging due to the poor resolution of the standalone muons used as probes. For the same reason, an enlarged fitting range is used. A Crystal Ball (and an additional Gaussian when needed to account for different event resolutions, eg for the MC fits) is chosen to describe the signal shape with all its parameters left to float. The background is described by a third order polynomial.

T&P mass fits for the tracking case are shown in Fig. 5.5, for the integrated data and MC samples. These illustrate the considerably large level of background involved, and the degraded mass resolution. Shown in Fig. 5.6 is the tracking efficiency as function of the probe muon and rapidity and event centrality. The MC is seen to overestimate the data, by about 5%.

Finally we summarize in Table 5.1 all the efficiency estimations as a function of centrality, based on the full data and simulation PbPbsamples.

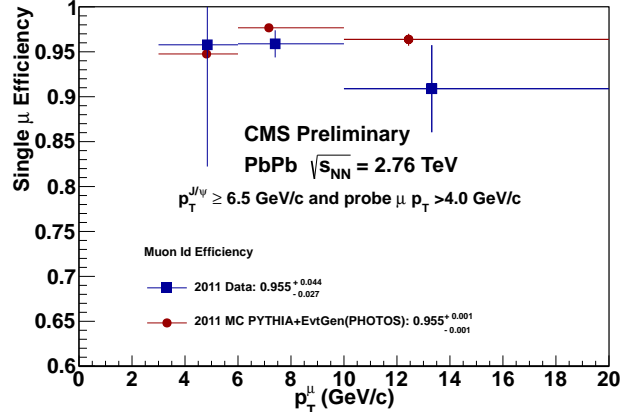


(a) Data

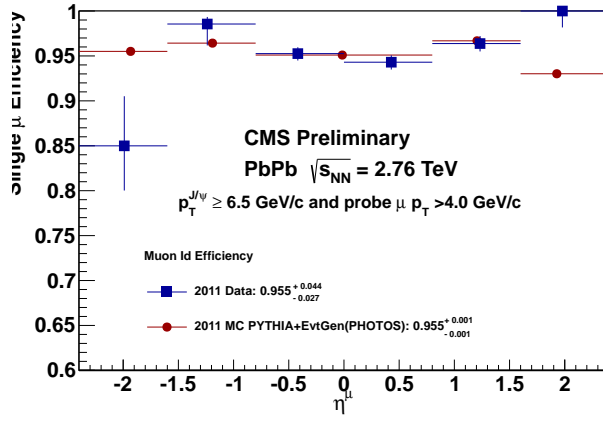


(b) Simulation

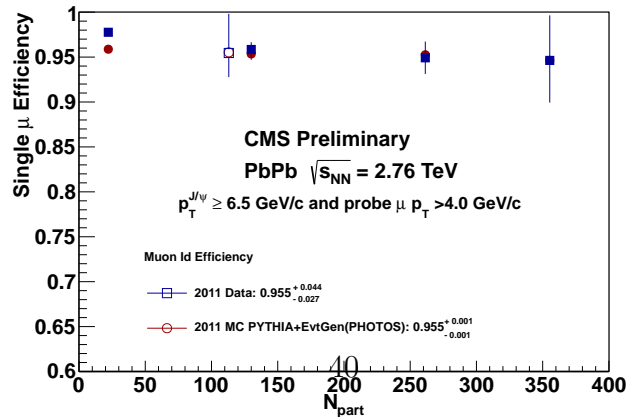
Figure 5.3: Examples of tag-probe pair mass fits for the muon identification



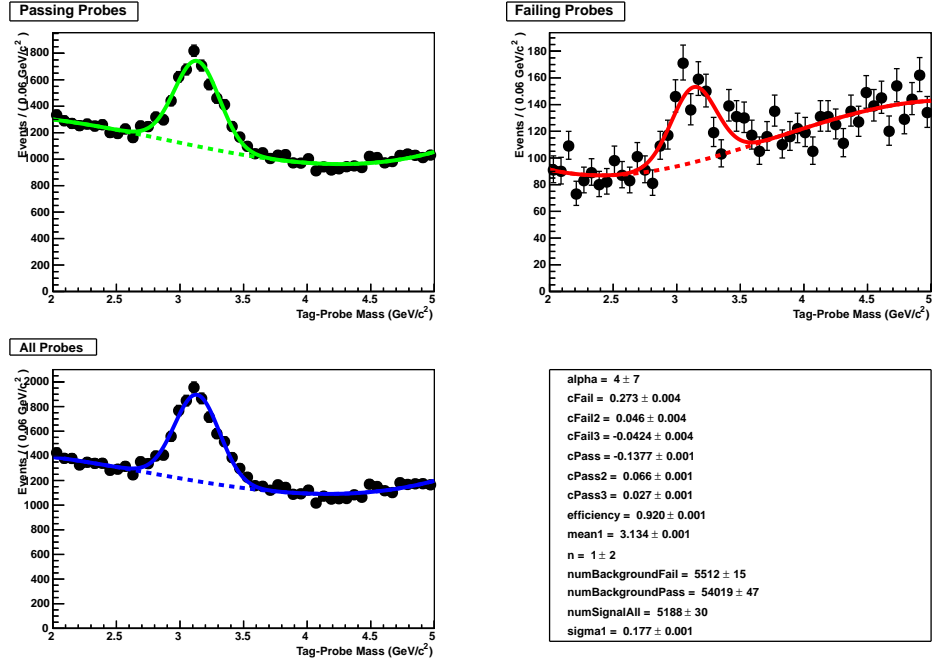
(a) Muon id efficiency dependence on muon p_T .



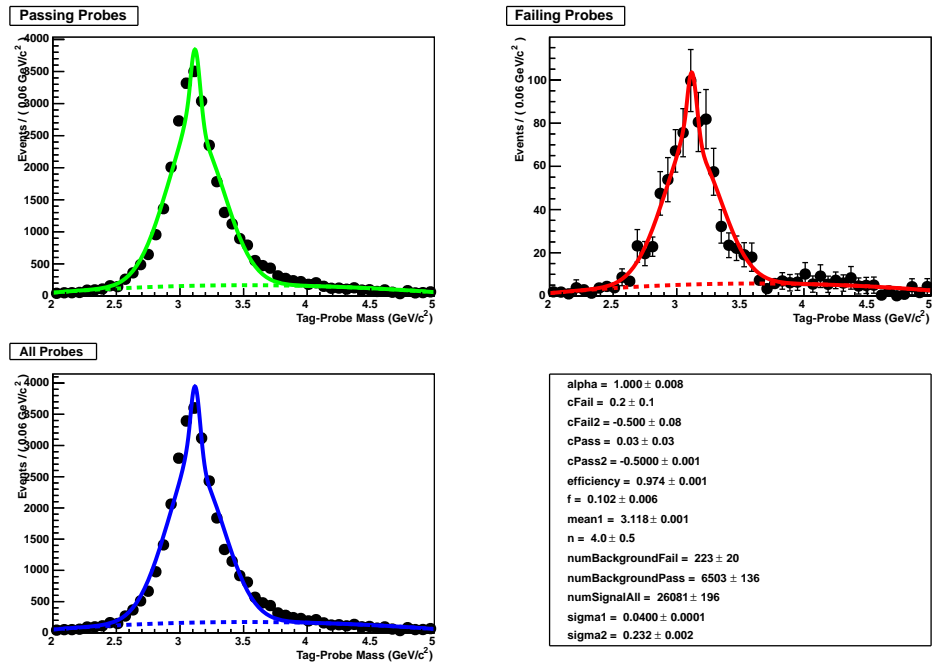
(b) Muon id efficiency dependence on muon η .



(c) Muon id efficiency dependence on event centrality.

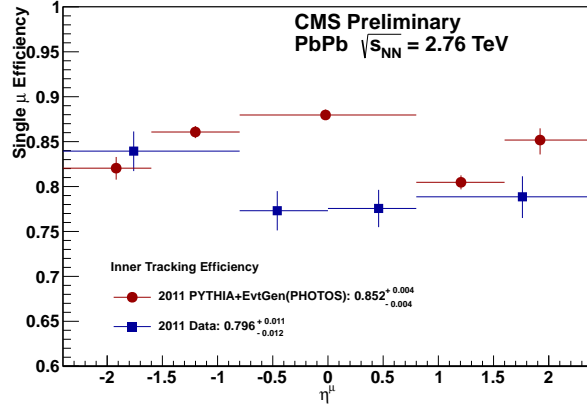


(a) Data

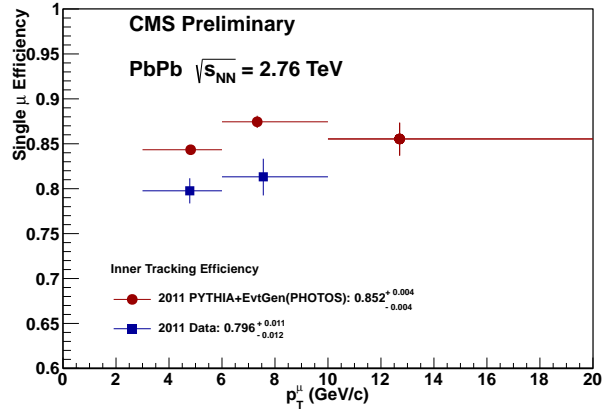


(b) Simulation

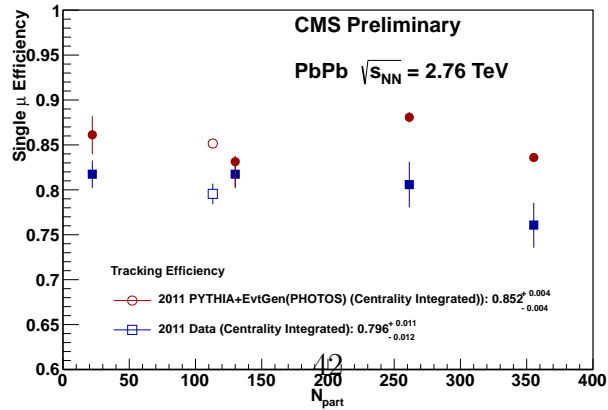
Figure 5.5: Examples of tag-probe pair mass fits for the inner tracking efficiency.



(a) Tracking efficiency dependence on muon η .



(b) Tracking efficiency dependence on muon p_T .



(c) Tracking efficiency dependence on event centrality.

Table 5.1: Tag and probe efficiency measurements in PbPb data and simulation; an acceptance cut $\mu > 4.0$ on the probe muons is applied; values are in percent, and errors are statistical only.

PbPb centrality	Muon Identification		Trigger		Tracking	
	MC	data	MC	data	MC	data
0-10%	94.6 ± 0.2	94.6 ± 5.0	93.9 ± 2.1	96.7 ± 0.5	83.6 ± 0.4	76.1 ± 2.5
10-20%	95.3 ± 0.3	94.9 ± 1.8	95.1 ± 4.8	96.9 ± 0.5	88.0 ± 0.6	80.6 ± 2.5
20-50%	95.3 ± 0.2	95.8 ± 2.5	94.4 ± 0.7	96.7 ± 0.4	83.1 ± 2.0	81.7 ± 1.5
50-100%	95.9 ± 0.6	97.8 ± 0.8	94.3 ± 0.7	96.8 ± 3.2	86.1 ± 2.0	81.7 ± 1.5
0-100%	95.5 ± 0.1	95.5 ± 4.4	94.3 ± 0.1	96.8 ± 0.2	85.2 ± 0.3	79.6 ± 1.2

Table 5.2 also summarizes the tag and probe results obtained from the pp data and MC datasets. These studies were performed in the analysis documented in Ref. [?]. While different selection criteria were employed therein, which prevents a direct comparison of results for pp and PbPb, this may be used for the purpose of data–simulation systematic estimation.

Table 5.2: Tag and probe efficiency measurements in pp data and simulation; an acceptance cut $\mu > 4.0$ on the probe muons is applied; values are in percent, and errors are statistical only; results from [?].

	Trigger		Tracking	
	MC	data	MC	data
pp	0.943 ± 0.002	0.925 ± 0.006	0.846 ± 0.010	0.82 ± 0.02

Chapter 6

Upper limits

The $\Upsilon(3S)$ peak is not significantly observed in the mass spectrum in the PbPb data. The significance of $\Upsilon(3S)$ peak is 0.86σ , evaluated from the profile likelihood ratio, as shown in Fig. 6.1. In this section we quantify the relative suppression of the 3S signal state.

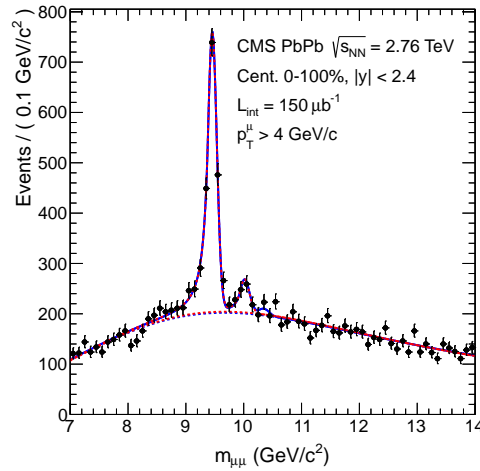


Figure 6.1: $\Upsilon(3S)$ significance, estimated via likelihood ratio, by allowing and disallowing $\Upsilon(3S)$ p.d.f. in two fits.

In some of the centrality bins the data is affected by large downward fluctuations of the background yielding negative yields for the signal $\Upsilon(3S)$. We proceed then to set upper limits for the signal 3S .

Approximate methods of confidence interval construction, in particular, the likelihood-ratio method, are often used in order to reduce computation. However, true confidence intervals can be obtained using the original (defining) Neyman construction [?]. Therefore we opted for the unified Feldman-Cousins (FC) approach since this treatment solves the problem whether to set an upper limit or two-sided intervals if the choice is based on the data alone as in our case.

As a cross check we also present a pure frequentist approach, the *modified*, or *conservative* CL_s criterion. Here, we use the ratio of p -values, $CL_s = CL_{sb}/CL_b$, instead of the numerator only, to set an upper limit on the single and double ratios involving the 3S. Finally other implementations based on 95% credible intervals are presented as cross-checks.

Single ratio R_3 limits

Instead on setting upper limits for the $\Upsilon(3S)$ signal per se we use the single ratio of the third peak over the first peak (R_3) in PbPb as our parameter of interest. The idea of the method can be formulated in terms of hypothesis testing in a frequentist approach. (for an explanation see [?]). We define H_b as the

alternative hypothesis that no signal 3S is present over the background (single ratio of zero) and H_{sb} the null hypothesis that the signal is indeed present. In order to quantify the degree in which each hypotheses are favored or excluded by the experimental observation one chooses a test-statistics which ranks the possible experimental outcomes. A commonly used test statistics consist as the ratio of the likelihood function in both hypotheses: $Q = L_{sb}/L_b$, for our study the test statistic of choice is $-2 \ln Q$.

We introduce the systematic uncertainties into the model via a nuisance parameter. Variation of such parameter corresponds to certain systematic uncertainty. The nuisance parameter is either profiled or marginalized depending on whether we are using the frequentist approach or the Bayesian one.

The computed 95% CL upper limit with FC is: 0.0737 ± 0.0014 . Cross checks based on alternative methods are provided in Appendix ??.

Double ratio χ_3 limits

The same statistical instruments shown above are also used to set the limits for double ratio χ_3 . Employing the Feldman Cousins technique, the upper limit at 95% C.L. is $\chi_3 \leq 0.173 \pm 0.021$, as represented in Fig. 6.3.

Using the profile likelihood calculator as cross-check, the 95% C.L. interval is $\chi_3 \in [0.042, 0.104]$, which is shown in figure Fig. 6.4.

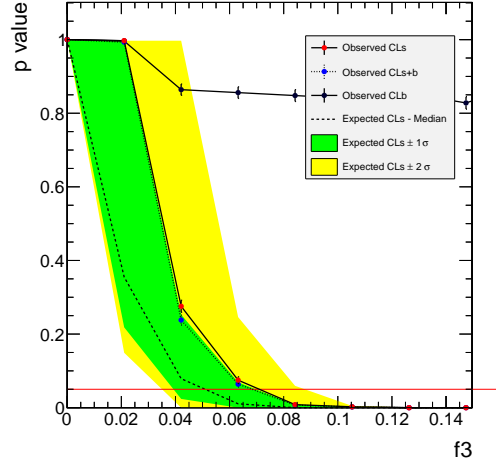


Figure 6.2: Upper limit results for R_3 in PbPb using the Feldman-Cousins method. Shown is a p -value scan using 1000 pseudo experiments for each scanned point. The 95% C.L. upper limit corresponds to the point where the observed CLs crosses the 0.05 horizontal/red line.

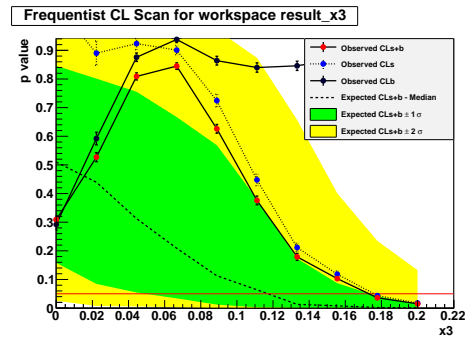


Figure 6.3: 95% interval on χ_3 with Feldman Cousins technique after including systematic uncertainties.

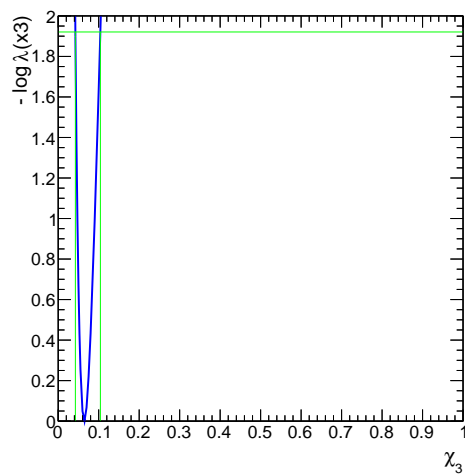


Figure 6.4: 95% interval on χ_3 with profile likelihood calculator not including systematic uncertainties.

Once the R_{AA} for the $\Upsilon(3S)$ signal is extracted from the simultaneous ML fit, we employ the Feldman-Cousins (FC) prescription to set a limit at 95% confidence level [?]. While the expected limit on the nuclear modification factor is close to a non-physical (≤ 0) result, the FC prescription guarantees a physically meaningful result and tells us how to smoothly transition from one-sided to two-sided limit. It uses a likelihood ratio as an ordering principle for selecting the acceptance region and creating confidence bands. The likelihood ratio is defined as the following:

$$Q(x) = \frac{P(x|R_{AA}(\Upsilon(3S))_0)}{P(x|R_{AA}(\Upsilon(3S))_{\max})}, \quad (6.1)$$

where $Q(x)$ is a likelihood ratio for given $R_{AA}(\Upsilon(3S))$, x , a given $R_{AA}(\Upsilon(3S))$ and finally $R_{AA}(\Upsilon(3S))_0$, and $R_{AA}(\Upsilon(3S))_{\max}$ is the $R_{AA}(\Upsilon(3S))$ for the maximum likelihood among all possible $R_{AA}(\Upsilon(3S))$ values.

For the centrality-integrated bin (0 -100%) the computed upper limit for the nuclear modification factor, $R_{AA}(\Upsilon(3S))$, using the FC method is about 0.095 (95% CL). This can be seen from Fig. 6.5, when the observed CL_s (red dots) crosses the horizontal threshold (red line). We generate 1000 pseudo experiments at each scanned point to discriminate the null hypothesis (no signal 3S is present) from the alternative (signal plus background) hypothesis.

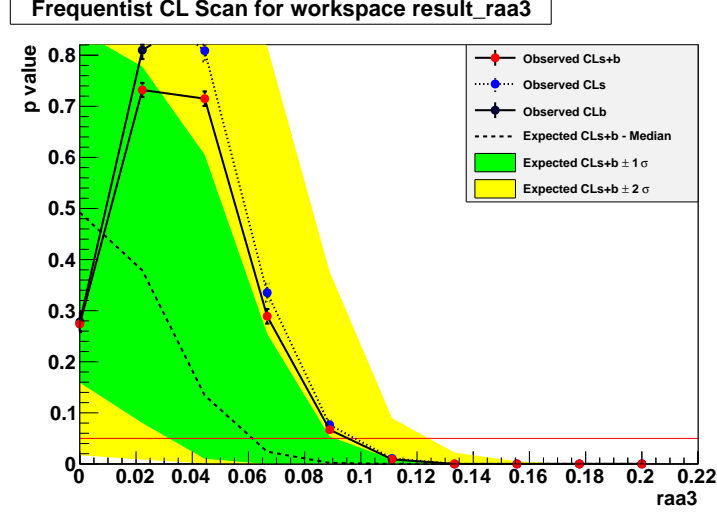
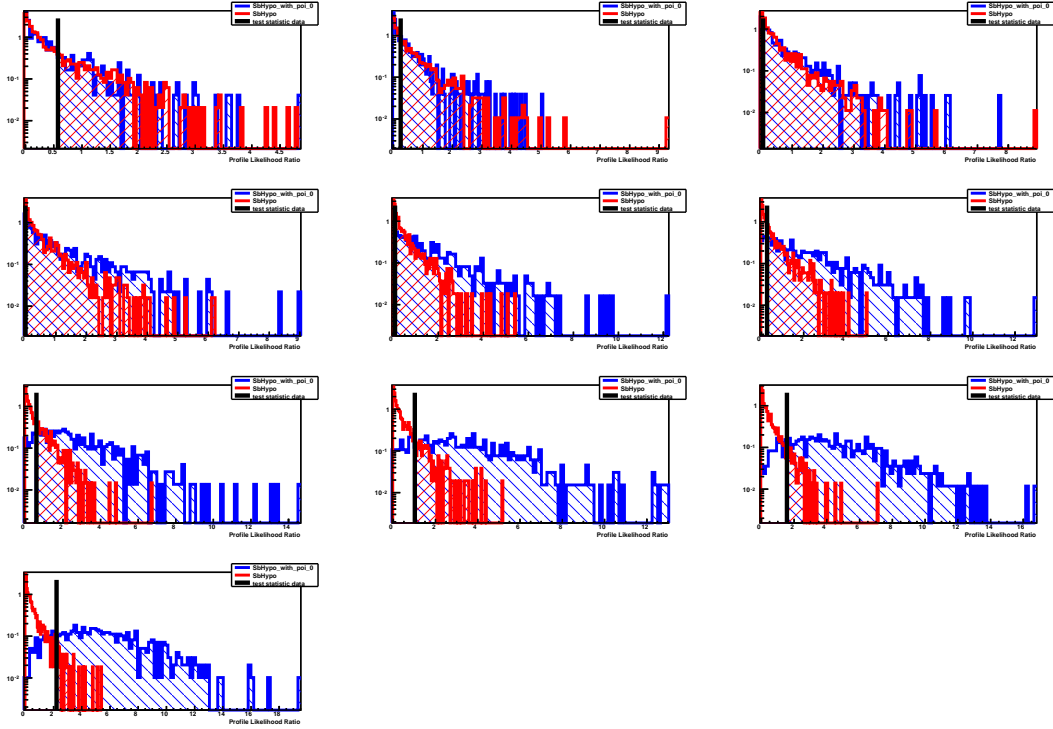


Figure 6.5: p -value scan for $R_{AA}(\Upsilon(3S))$ using the Feldman-Cousins technique.

The systematics uncertainties on the $p\bar{p}$ luminosity, the nuclear overlap function T_{AA} and the efficiency ratios as well as the uncertainties for the background shape and the signal FSR need to be taken into consideration when setting the upper limit. We fold in these systematics, which were previously specified, via nuisance parameters in the fit.

Figure 6.7 shows cross checks using the profile likelihood ratio implementation, where an $R_{AA}(\Upsilon(3S))$ upper limit of about 0.0952 (95% CL) is obtained. Notice that both results are consistent within uncertainties. The results for the two implementations are summarized in Table 6.1.



(a) Pseudo-experiments for null and alternative hypotheses and using likelihood ratio test statistics.

Figure 6.6: A thousand pseudo-experiments for each of the ten points scanned. H_{sb} ; red curve, H_b blue curve and black line is the test statistic. As we increase our parameter of interest it is easier to differentiate between the two hypotheses and the area under the red curve becomes smaller than the area under the blue curve.

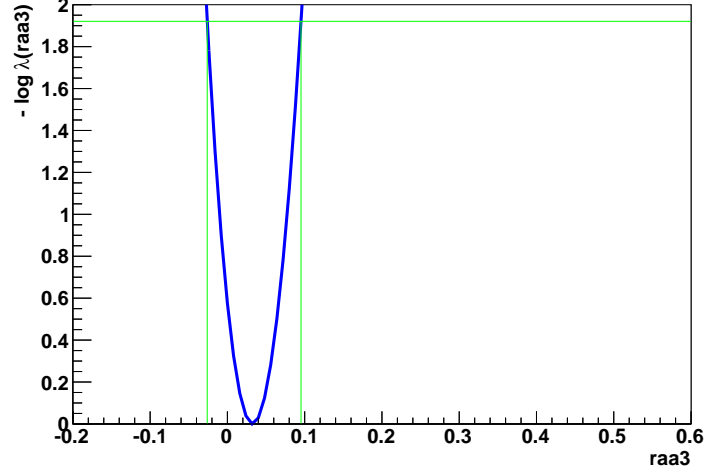


Figure 6.7: Profiled likelihood ratio. It shows the confidence interval at 95% confidence level.

Since we are interested in the suppression pattern of the three Υ states and because the errors for the Raa for the $\Upsilon(1S)$ and $\Upsilon(2S)$ have been calculated with a 1σ error, we also set the upper limits at a 68% confidence level.

In this scenario the upper limit using the Feldman Cousins technique is

$$R_{AA}(\Upsilon(3S)) \leq 0.064 \pm 0.001 \text{ at } 68\% \text{ confidence level.}$$

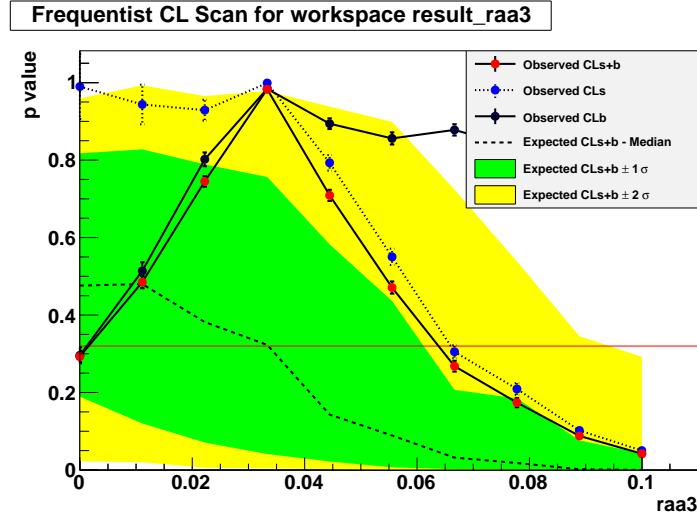


Figure 6.8: p -value scan for $R_{AA}(\Upsilon(3S))$ using the Feldman-Cousins technique at 68 % confidence level.

Table 6.1: $R_{AA}(\Upsilon(3S))$ upper limits. (*Note: being updated*)

centrality	best fit value	95% C.L upper limit	
		Feldman-Cousins	profile likelihood ratio
0 - 100%	0.032 ± 0.031	0.09506 ± 0.00130	0.0952

We have used two Bayesian implementations to cross check our results. The first Bayesian calculation is using numeric integration assuming a flat prior to derive a one sided 95% credible interval and the second one is using Markov Chain Monte Carlo sampling which is based on the Metropolis-Hastings algorithm [?].

For the centrality integrated bin (0 -100%) the computed upper limit for the single ratio of 3S/1S using the Feldman-Cousins method is $R_3 = 0.0695 \pm 0.0004$ which can be seen from Fig. 6.2. when the observed CL_s (red dots) crosses the horizontal threshold (red line). In Fig. 6.9 we present the upper limits for all the centrality bins as a function of the number of participants. The two lowest values for the upper limits were found in the centrality bins where we had negative yields from the fitted results. These upper limits are indeed positive as expected. Figure 6.10 shows cross checks using different implementations. Figs. 6.10(a) and 6.10(b) use CL_s and its asymptotic approximation, and Figs. 6.10(c), 6.10(d) use Bayesian numeric integration and Markov Chain Montecarlo, respectively. Notice that all results are consistent within uncertainties. Finally, in Fig. 6.11, we show Bayesian results in the (30-40%) centrality bin where we found negative ratios. The upper limits found for the different centrality bins are tabulated in Tables 6.2 and 6.3.

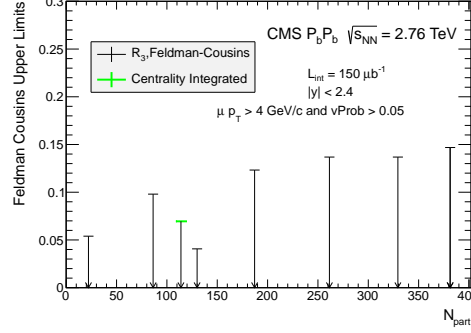


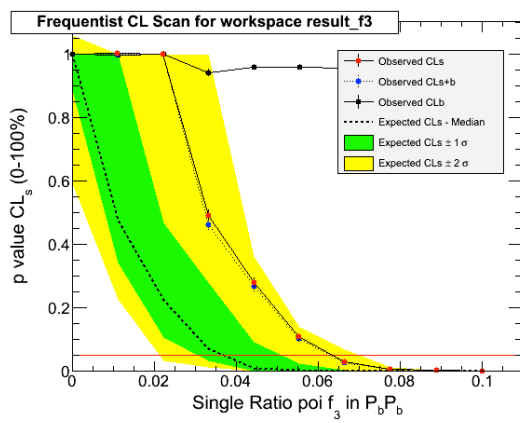
Figure 6.9: Upper limit results using the Feldman-Cousins method on R_3 in PbPb, evaluated for the different centrality bins. (*Note: being updated*)

Table 6.2: Single-ratio upper limits. (*Note: being updated*)

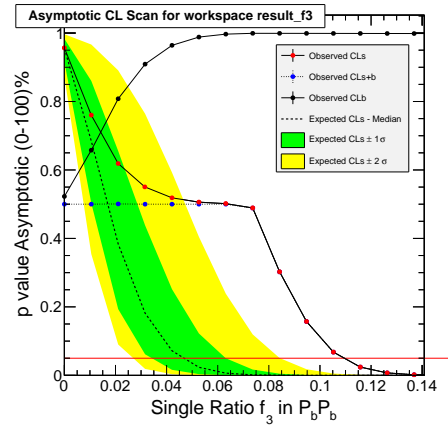
	R_3	Feldman-Cousins	frequentist scan CL_s	asymptotic scan
0 - 5%	0.043 ± 0.051	0.147 ± 0.003	0.143 ± 0.005	0.129
5 - 10%	0.018 ± 0.055	0.1368 ± 0.0009	0.2222 ± 0.0002	0.124
10 - 20%	0.0062 ± 0.0352	0.1390 ± 0.0009	0.3129 ± 0.0005	0.074
20 - 30%	0.052 ± 0.036	0.1232 ± 0.0006	0.110 ± 0.0003	0.11
30 - 40%	-0.046 ± 0.045	0.0407 ± 0.0001	0.065 ± 0.011	0.063
40 - 50%	0.23 ± 0.070	0.0980 ± 0.0003	0.364 ± 0.003	0.35
50 - 100%	-0.069 ± 0.061	0.054 ± 0.0002	0.081 ± 0.005	0.084
0 - 100%	0.032 ± 0.019	0.0695 ± 0.0004	0.0638 ± 0.00006	0.0631

Table 6.3: Single-ratio credible intervals: Bayesian cross checks. (*Note: being updated*)

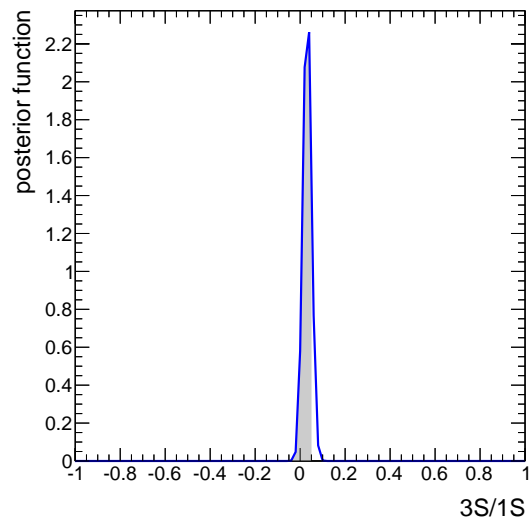
	R_3	Bayesian calculator	$MCMC$
0 - 5%	0.043 ± 0.051	$[-1, 0.12]$	$[-1, 0.14]$
5 - 10%	0.018 ± 0.055	$[-1, 0.091]$	$[-1, 0.47]$
10 - 20%	0.0062 ± 0.0352	$[-1, 0.051]$	$[-1, 0.070]$
20 - 30%	0.052 ± 0.036	$[-1, 0.091]$	$[-1, 0.11]$
30 - 40%	-0.046 ± 0.045	$[-1, 0.010]$	$[-1, 0.028]$
40 - 50%	0.23 ± 0.070	$[-1, 0.33]$	$[-1, 0.41]$
50 - 100%	-0.069 ± 0.061	$[-1, 0.010]$	$[-1, 0.062]$
0 - 100%	0.032 ± 0.019	$[-1, 0.051]$	$[-1, 0.062]$



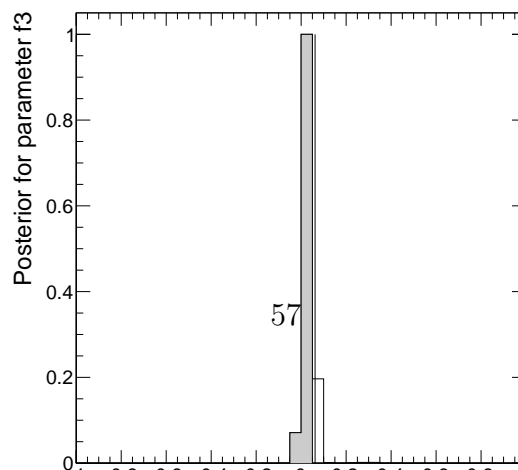
(a) Observed CLs crosses the 0.05 red line

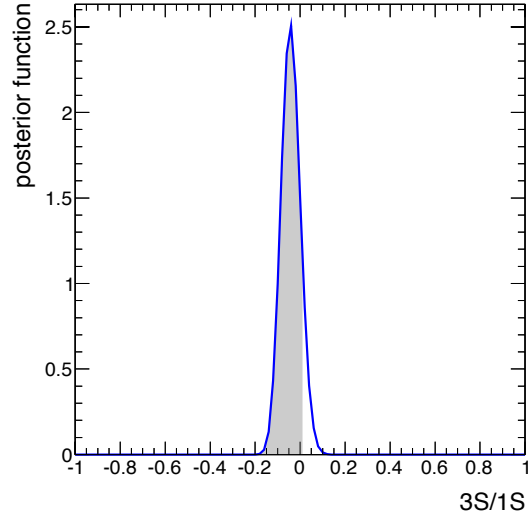


(b) Asymptotic approach using Asimov test statistics

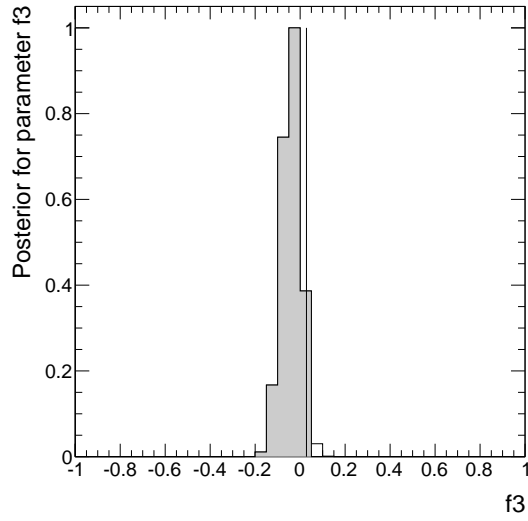


(c) Bayesian posterior





(a) Bayesian posterior



(b) MC Markov Chain posterior

Figure 6.11: Bayesian results for 40-50% centrality bin. Figures 6.11(a), 6.11(b): Bayesian Numeric Calculator and Montecarlo Markov Chain. (*Note: being updated*)

Chapter 7

Final results

Bottomonium suppression in PbPb collisions is studied in this section by measuring the ratios of observed yields of excited Υ states relative to the ground $\Upsilon(1S)$ state, with the $150\mu b^{-1}$ 2011 PbPb data. The suppression is inferred by performing a comparison of the ratios measured in PbPb against the pp reference. Dependencies on the centrality of the PbPb collision are explored.

The data samples, reconstruction and selection criteria are described in Sections ?? and ?. The parameters of interest are extracted from the data samples directly via an extended unbinned maximum likelihood fit to the dimuon invariant-mass spectra, described in Section ??.

7.0.7 Single ratio measurement

The following ratios of observed yields of Υ excited states relative to the ground state are studied:

$$R_{23} \equiv \frac{N(\Upsilon(2S)) + N(\Upsilon(3S))}{N(\Upsilon(1S))}, \quad (7.1)$$

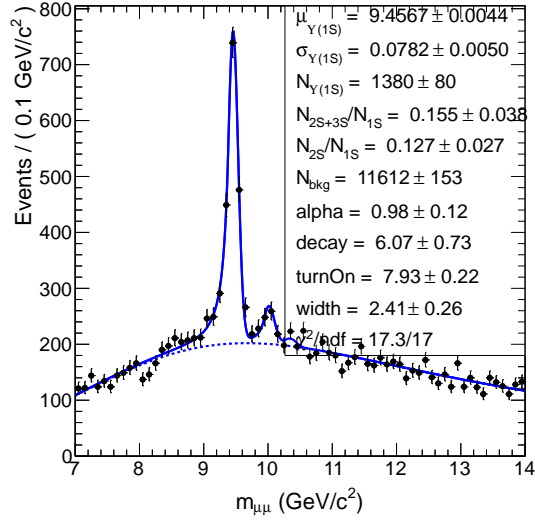
$$R_2 \equiv \frac{N(\Upsilon(2S))}{N(\Upsilon(1S))}, \quad (7.2)$$

$$R_3 \equiv \frac{N(\Upsilon(3S))}{N(\Upsilon(1S))}. \quad (7.3)$$

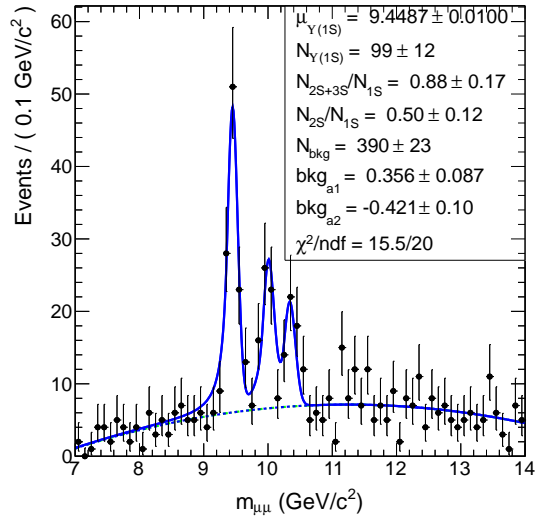
In addition to the combined excited-to-ground ratio, R_{23} , the current statistics allow to extract the separate 2S and 3S ratios, R_2 and R_3 . No evidence for the $\Upsilon(3S)$ state is found in the PbPb data, and the corresponding ratio is studied in Sec. ??.

These ratios are measured from fits to the PbPb and pp datasets, separately performed. The nominal $p_T > 4.0$ cut is used. These fits are displayed in Fig. 7.1. The fit results are shown in Table ?? for the PbPb data, and in Table ?? for the pp (2.76 TeV) dataset.

Various systematic variations of the fit model are performed, to further establish the stability of the results. For the fit to the PbPb data, the following variations are considered:



(a) Fit to the PbPb data



(b) Fit to the pp data

Figure 7.1: Nominal mass fits, performed separately to the PbPb($150\mu b^{-1}$) and pp($231nb^{-1}$) full datasets.

- like-sign background modeling: the background model is formed of two components, given by the like-sign distribution and a second order polynomial; the PDF from the like-sign data is obtained from a fit employing the erf * exp model (Fig 7.2(g))
- like-sign background modeling: the background model is formed of two components, given by the like-sign distribution and a second order polynomial; the PDF from the like-sign data is obtained from the RooKeysPdf smoothing method (Fig 7.2(d))
- track-rotation background modeling: the background model is formed of two components, given by the track-rotation distribution and a second order polynomial; the PDF from the track-rotation data is obtained from a fit employing the erf * exp model (Fig 7.2(h) and 7.2(i))
- track-rotation background modeling: the background model is formed of two components, given by the track-rotation distribution and a second order polynomial; the PDF from the track-rotation data is obtained from the RooKeysPdf smoothing method (Fig 7.2(e) and 7.2(f))
- the CB signal tail parameters are fixed ($\alpha = 1.4$, from high-statistics data as in Table 4.1) (Fig 7.2(a))
- the resolution is fixed ($\sigma_{1S} = 92$) (Fig 7.2(b))

-
- the signal shape parameters are fixed ($\alpha = 1.4, n = 2.3, \sigma_{1S} = 92$) (Fig 7.2(c))

For the fit to the pp data, these variations are considered:

- the CB signal tail parameters are fixed ($\alpha = 1.4$, from high-statistics data as in Table 4.1)
- the resolution is fixed ($\sigma_{1S} = 92$)
- the signal shape parameters are fixed ($\alpha = 1.4, n = 2.3, \sigma_{1S} = 92$)
- like-sign background modeling: the background model is formed of two components, given by the like-sign distribution and a second order polynomial; the PDF from the like-sign data is obtained from a fit employing the erf * exp model
- like-sign background modeling: the background model is formed of two components, given by the like-sign distribution and a second order polynomial; the PDF from the like-sign data is obtained from the RooKeysPdf smoothing method
- error function for background shape

The associated systematic uncertainties are summarized in Table 7.1 for PbPb, and in Table 7.2 for *pp*. From the several variations, two estimates of the systematic uncertainty are provided: (i) the quadratic-mean deviation relative to the

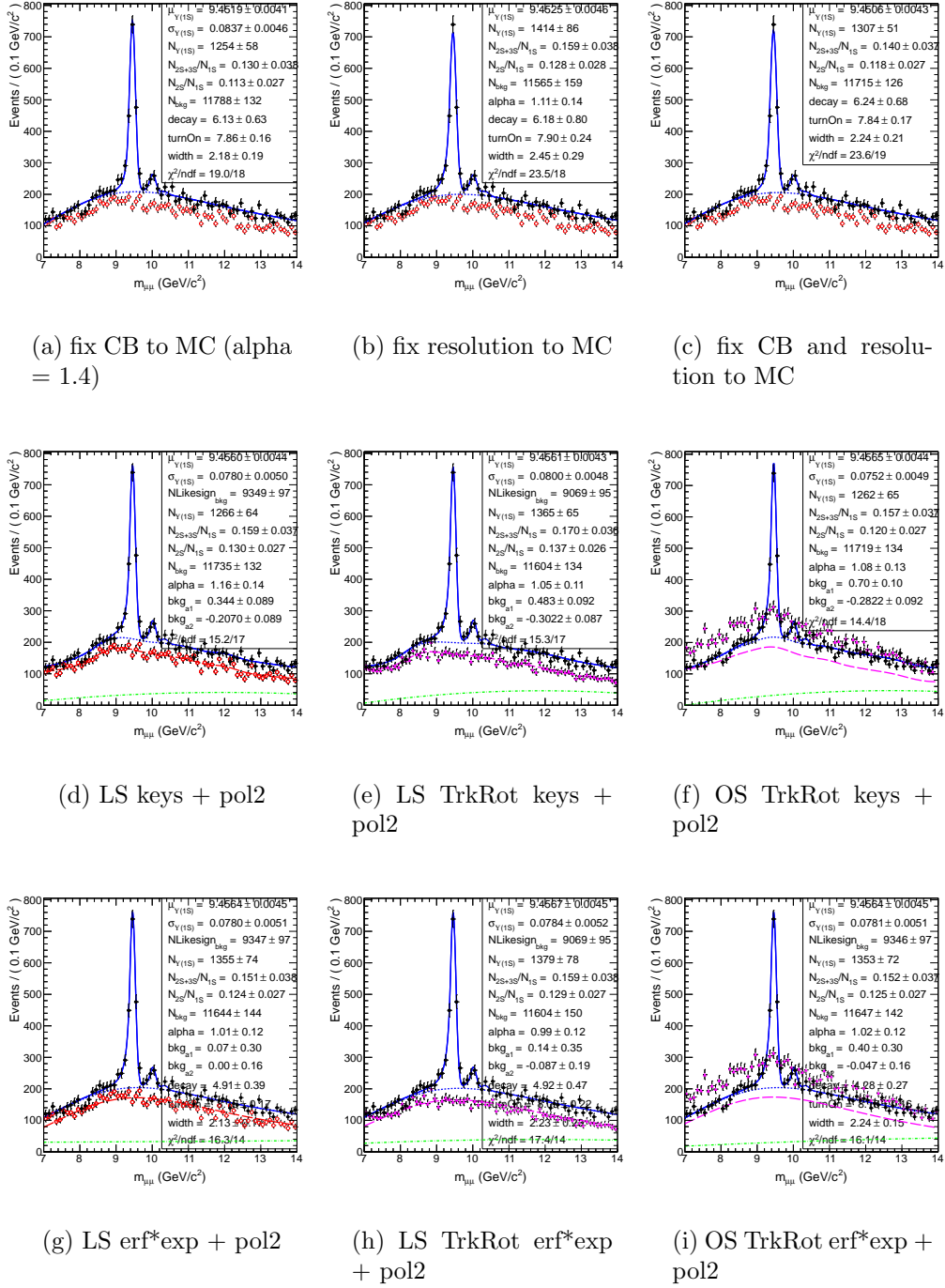


Figure 7.2: PbPb fit model variations ($150\mu b^{-1}$).

nominal central value, RMS (schematically, $\sqrt{(\sum \text{variation} - \text{nominal})^2 / (n - 1)}$);
and (ii) the largest deviation. The latter is used as the estimated systematic uncertainty.

Table 7.1: Summary of single-ratio results, for the PbPb dataset.

	$^{\mu} > 4$, Cent. 0-100%		
	R_{23}	R_2	R_1
nominal (erf*exp)	0.155 ± 0.038	0.127 ± 0.027	0.027 ± 0.007
systematic variations:			
like-sign (LS) keyspdf + pol.2	0.159 ± 0.037	0.130 ± 0.027	0.029 ± 0.007
LS erf*exp + pol.2	0.151 ± 0.038	0.124 ± 0.027	0.027 ± 0.007
opposite-sign (OS) Track Rotation (TR) keyspdf + pol.2	0.157 ± 0.037	0.120 ± 0.027	0.037 ± 0.007
OS TR erf*exp + pol.2	0.152 ± 0.037	0.125 ± 0.027	0.025 ± 0.007
fix CB tail from MC (alpha = 1.4)	0.130 ± 0.038	0.113 ± 0.027	0.017 ± 0.007
fix resolution from MC (92)	0.159 ± 0.038	0.128 ± 0.028	0.031 ± 0.007
fix both CB and resolution from MC	0.140 ± 0.037	0.118 ± 0.027	0.022 ± 0.007
fit systematic (RMS)	0.011	0.007	0.007
fit systematic (largest variation)	0.026	0.016	0.007
other checks:			
LS Track Rotation (TR) keyspdf + pol.2	0.170 ± 0.036	0.137 ± 0.026	0.033 ± 0.007
LS TR erf*exp + pol.2	0.159 ± 0.038	0.129 ± 0.027	0.030 ± 0.007
nominal simultaneous fit (erf*exp)	0.143 ± 0.038	0.119 ± 0.027	0.024 ± 0.007

7.0.8 Centrality dependence

Effects induced by the hot medium are expected to display, in general, a dependence on the centrality of the collision – the effect is more accentuated for the most central collision events, and approaching the most peripheral events tend asymptotically towards the results expected in the absence of medium effects.

The pp collision results are taken as reference for absence of nuclear effects.

Table 7.2: Summary of single-ratio results for the 2.76 TeV dataset.

	$\mu > 4$		
	R_{23}	R_2	R_3
nominal (pol2; signal pdf fixed from PbPb)	0.88 ± 0.17	0.50 ± 0.12	0.38 ± 0.10
systematic variations:			
fix CB tail from MC	0.85 ± 0.16	0.49 ± 0.11	0.36 ± 0.19
fix resolution from MC	0.89 ± 0.16	0.49 ± 0.12	0.40 ± 0.20
fix both CB and resolution	0.87 ± 0.16	0.49 ± 0.11	0.38 ± 0.19
erf*exp	0.86 ± 0.16	0.49 ± 0.11	0.37 ± 0.19
LS keyspdf + pol.2	0.84 ± 0.17	0.48 ± 0.12	0.36 ± 0.21
LS erf*exp + pol.2	0.87 ± 0.16	0.49 ± 0.12	0.38 ± 0.20
fit systematic (RMS)	0.023	0.012	0.015
fit systematic (largest variation)	0.051	0.024	0.035
nominal simultaneous fit (pol2)	0.97 ± 0.19	0.56 ± 0.13	0.41 ± 0.11

We repeat the single ratio measurement, by splitting the PbPb dataset in ranges of the collision centrality. The mass fit results are shown in Figures 7.3.

The systematic uncertainties are evaluated for the nominal selection, and summarized in Table 7.0.8. The corresponding differential results are displayed in Fig. 7.4. In these plots, the single ratio values are normalized by the central value of the measurement performed using the data. Note these normalization values depend on the threshold case, and are obtained from the fit to the data with constrained signal shape from MC, displayed in Table 7.2. Uncertainties on the single-point measurement are not included, as such common uncertainty factor is not relevant for point-to-point comparison in this plot showing the double ratio trend with N_{part} . Some error bars in Fig. 7.4 reach negative values, so we refine this using Feldman-Cousins limit calculation as shown in Fig. 7.5.

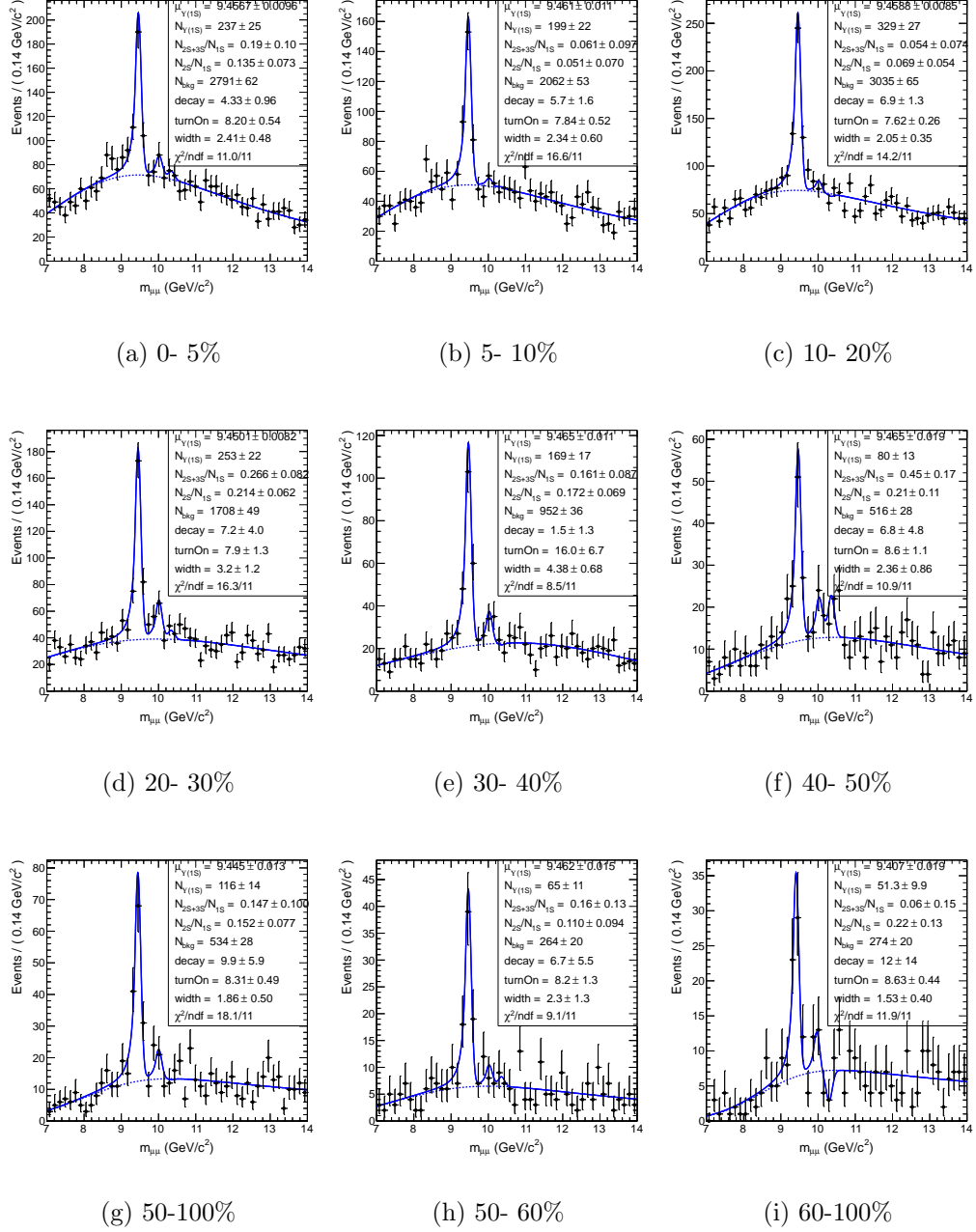
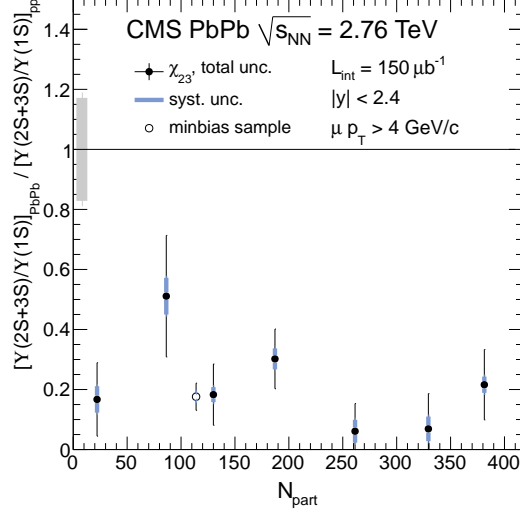


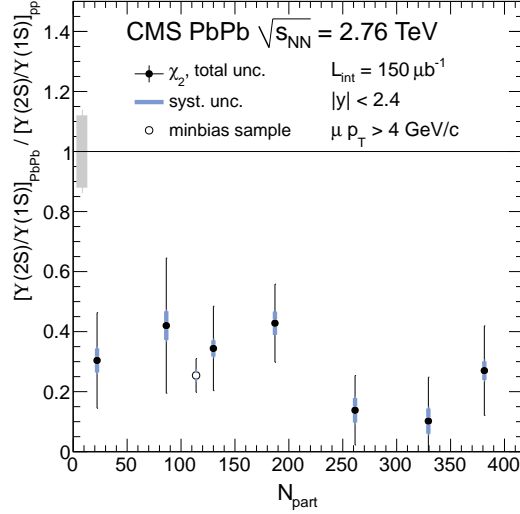
Figure 7.3: Centrality dependence of the PbPb single ratio, for $\mu > 4.0$. ($150\mu\text{b}^{-1}$).

[lh] Summary of single-ratio centrality dependent results.					
	0-5%	5-10%	10-20%	20-30%	30-40%
R_{23} ($\mu > 4.0$)					
nominal result	0.190 ± 0.100	0.061 ± 0.097	0.054 ± 0.074	0.266 ± 0.082	0.161 ± 0.074
systematic variations:					
LS keyspdf + pol.2	0.220 ± 0.099	0.009 ± 0.097	0.030 ± 0.075	0.246 ± 0.079	0.125 ± 0.074
TR keyspdf + pol.2	0.237 ± 0.097	-0.011 ± 0.093	0.109 ± 0.070	0.200 ± 0.084	0.151 ± 0.074
LS erf*exp + pol.2	0.189 ± 0.104	0.060 ± 0.097	0.029 ± 0.079	0.251 ± 0.082	0.125 ± 0.074
TR erf*exp + pol.2	0.187 ± 0.105	0.057 ± 0.100	0.078 ± 0.073	0.263 ± 0.080	0.151 ± 0.074
fix CB tail to MC	0.186 ± 0.109	0.039 ± 0.102	0.015 ± 0.083	0.234 ± 0.081	0.158 ± 0.074
fix resolution to MC	0.186 ± 0.101	0.051 ± 0.097	0.088 ± 0.076	0.287 ± 0.082	0.183 ± 0.074
fix both CB and resolution	0.162 ± 0.108	0.037 ± 0.099	0.039 ± 0.073	0.254 ± 0.081	0.151 ± 0.074
fit systematic:					
RMS	0.024	0.036	0.033	0.031	0.031
largest variation	0.047	0.072	0.055	0.066	0.055
R_2 ($\mu > 4.0$)					
nominal result	0.135 ± 0.078	0.051 ± 0.070	0.069 ± 0.054	0.214 ± 0.062	0.172 ± 0.054
systematic variations:					
LS keyspdf + pol.2	0.154 ± 0.074	0.022 ± 0.070	0.047 ± 0.055	0.205 ± 0.062	0.150 ± 0.054
TR keyspdf + pol.2	0.164 ± 0.072	0.008 ± 0.068	0.102 ± 0.053	0.171 ± 0.064	0.172 ± 0.054
LS erf*exp + pol.2	0.134 ± 0.075	0.052 ± 0.071	0.056 ± 0.056	0.204 ± 0.063	0.152 ± 0.054
TR erf*exp + pol.2	0.133 ± 0.075	0.050 ± 0.071	0.080 ± 0.054	0.211 ± 0.062	0.165 ± 0.054
fix CB tail to MC	0.136 ± 0.077	0.039 ± 0.071	0.044 ± 0.057	0.194 ± 0.060	0.176 ± 0.054
fix resolution to MC	0.127 ± 0.074	0.046 ± 0.071	0.087 ± 0.056	0.224 ± 0.063	0.189 ± 0.054
fix both CB and resolution	0.116 ± 0.077	0.038 ± 0.070	0.057 ± 0.052	0.206 ± 0.061	0.171 ± 0.054
fit systematic:					
RMS	0.015	0.021	0.021	0.019	0.019
largest variation	0.029	0.043	0.033	0.043	0.033

No clear dependence can be inferred within the statistical precision offered by the data. We also note that the most peripheral bin in PbPband the pp preference do not necessarily match, both because a fully peripheral bin is not accessible given limited statistics in the data, and as a consequence of complexity of the underlying phenomena.

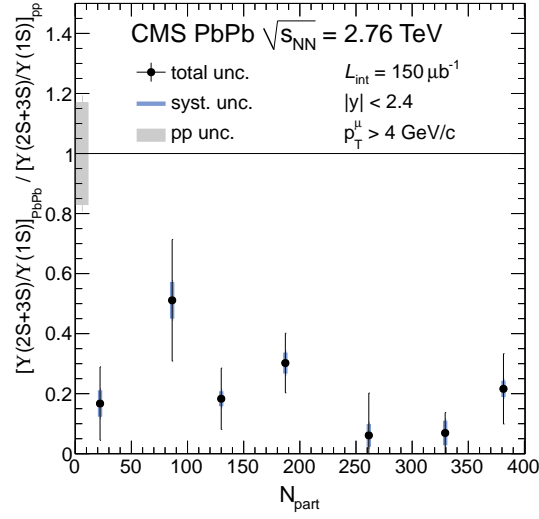


(a) $\chi_{23}, \mu > 4.0$

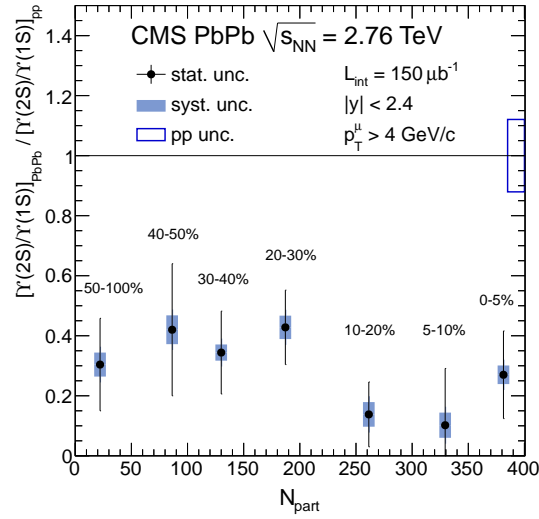


(b) $\chi_2, \mu > 4.0$

Figure 7.4: Centrality dependence of the double ratios χ_{23} and χ_2 ; the PbPb statistical and systematic uncertainties are included; the graphs are normalized by the corresponding pp single-ratio central values; pp uncertainties are represented by gray box at unity, and are excluded from the data points as they do not affect point-to-point trend comparison. ($150\mu\text{b}^{-1}$).



(a) $\chi_{23}^{\mu} > 4.0$



(b) $\chi_2^{\mu} > 4.0$

Figure 7.5: Replace the negative error bars in Fig. 7.4 with Feldman-Cousins limits.

7.0.9 Double ratio measurement

Here we study the comparison of the single ratios measured in PbPb and . Such a double-ratio is given by

$$\chi_{23} \equiv \frac{R_{23|\text{PbPb}}}{R_{23|}} = \frac{[N(\Upsilon(2\text{S}) + \Upsilon(3\text{S}))/N(\Upsilon(1\text{S}))]_{\text{PbPb}}}{[N(\Upsilon(2\text{S}) + \Upsilon(3\text{S}))/N(\Upsilon(1\text{S}))]} , \quad (7.4)$$

$$\chi_2 \equiv \frac{R_{2|\text{PbPb}}}{R_{2|}} = \frac{[N(\Upsilon(2\text{S}))/N(\Upsilon(1\text{S}))]_{\text{PbPb}}}{[N(\Upsilon(2\text{S}))/N(\Upsilon(1\text{S}))]} , \quad (7.5)$$

$$\chi_3 \equiv \frac{R_{3|\text{PbPb}}}{R_{3|}} = \frac{[N(\Upsilon(3\text{S}))/N(\Upsilon(1\text{S}))]_{\text{PbPb}}}{[N(\Upsilon(3\text{S}))/N(\Upsilon(1\text{S}))]} . \quad (7.6)$$

No evidence for the $\Upsilon(3\text{S})$ state is found in the PbPb data, and the corresponding ratio is studied in Sec. ??.

Several effects, and associated uncertainties, cancel out in the computation of these doubly normalized observables, including efficiency and acceptance correction factors.

The PbPb and data samples are fitted simultaneously, and the double ratios are directly extracted as fit parameters. The background is described by the nominal $\text{erf} \cdot \text{exp}$ model, in the case of the PbPb dataset. For the pp dataset, in view of the smaller statistics, a simpler background model is employed, namely a second order polynomial (that is, the same model and dataset as in previous publication [?]). The signal shape parameters are common, while the backgrounds float separately in the simultaneous fit. The fit projections are shown in Figures 7.6.

The double-ratio results and systematic uncertainties are summarized in Table 7.3. For the signal fit function, we tried 7 different systematic variations (Table 7.3):

- the CB signal tail parameters are fixed ($\alpha = 1.4$, from high-statistics data as in Table 4.1)
- the $\Upsilon(1S)$ mass resolution is fixed to Monte Carlo (92)
- fix both the CB parameters and mass resolution
- let the CB tail float separately in pp and PbPb samples (it is shared for nominal)
- let the resolution float separately in pp and PbPb samples (it is shared for nominal)
- let both the CB tail and resolution float separately in pp and PbPb samples (they are shared for nominal)
- share $\Upsilon(1S)$ mass mean in pp and PbPb samples (they float separately in the nominal configuration).

For the background function, we tried the following three sets of variations (Table 7.3):

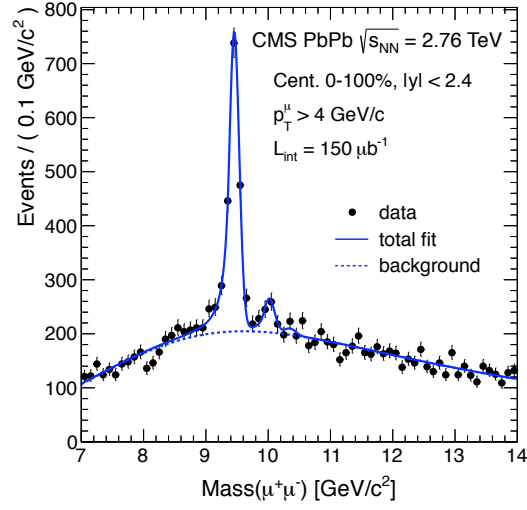
-
- keep the second order polynomial for pp, but vary the PbPb fit with 4 different pdfs
 - keep the erf*exp function for PbPb, but vary the pp fit with 4 different pdfs
 - vary both PbPb and pp background pdfs at the same time

The systematic uncertainties associated to the signal and background modeling are estimated as the RMS, computed relative to the nominal fit value, for the corresponding set of variations described above. The total systematic uncertainty is obtained as the quadrature sum of these two sources. The systematic uncertainties on the double ratios are detailed in Table 7.3.

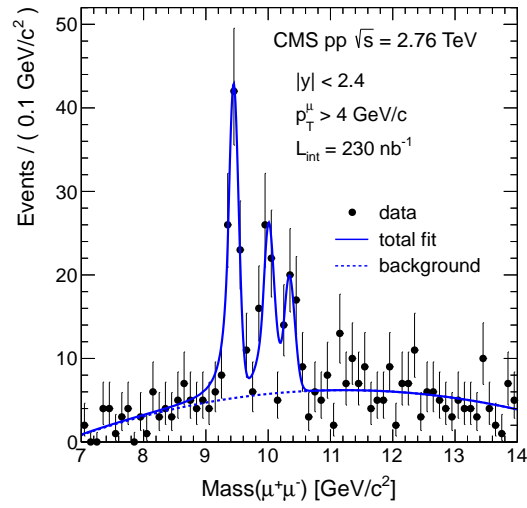
7.0.10 Kinematic dependences

The single-ratio and double-ratio measurements are performed in bins of \dimuon_{rap} and transverse momentum, for the nominal (> 4.0) selection. The fits to the data are shown in Figures 7.7 and 7.8. The background level and shape are seen to vary considerably in the different regions, as expected. For example, the kinematic effect due to the μ selection threshold is more noticeable for low \dimuon_{rap} and high rapidity regions, with softer μ spectra.

The double-ratio results are represented in the graphs in Fig. 7.9. Due to the limited statistics in the pp_{sample} , the statistical precision available does not



(a) PbPbprojection



(b) *pp*projection

Figure 7.6: Simultaneous fit to the PbPb($150\mu\text{b}^{-1}$) and *pp*(231nb^{-1}) datasets, for $\mu > 4.0$.

allow to infer possible dependencies of the double ratio on the inspected kinematic variables.

7.0.11 Significance

Double ratio significance

Here we attempt to quantify the significance of the observed relative suppression of the excited-to-ground states, estimated through the double ratios χ_{23} and χ_2 .

The nominal method employed consists of employing the profile likelihood calculator, implemented in the Root/RooStats package (`ProfileLikelihoodCalculator`). The null hypothesis is that χ_{23} and χ_2 are unity. Utilizing the nominal fit procedure, and ignoring systematic uncertainties, the obtained p-value of our result with respect to the null hypothesis corresponds to 6.3σ . The projections of the fit overlaid with the fit under the null hypothesis is shown in Fig. 7.10.

The propagation of systematic uncertainties is challenging. In particular, the various systematic variations considered cannot be readily expressed as nuisance parameters of the nominal fit model. Instead, we adopt for this purpose a modified fit configuration, identical to our nominal except that we restrict the fitting range to $(8, 14)$. This has the effect of increasing the statistic fit uncertainties on the parameters of interest (ie the double ratios) to the level expected for the

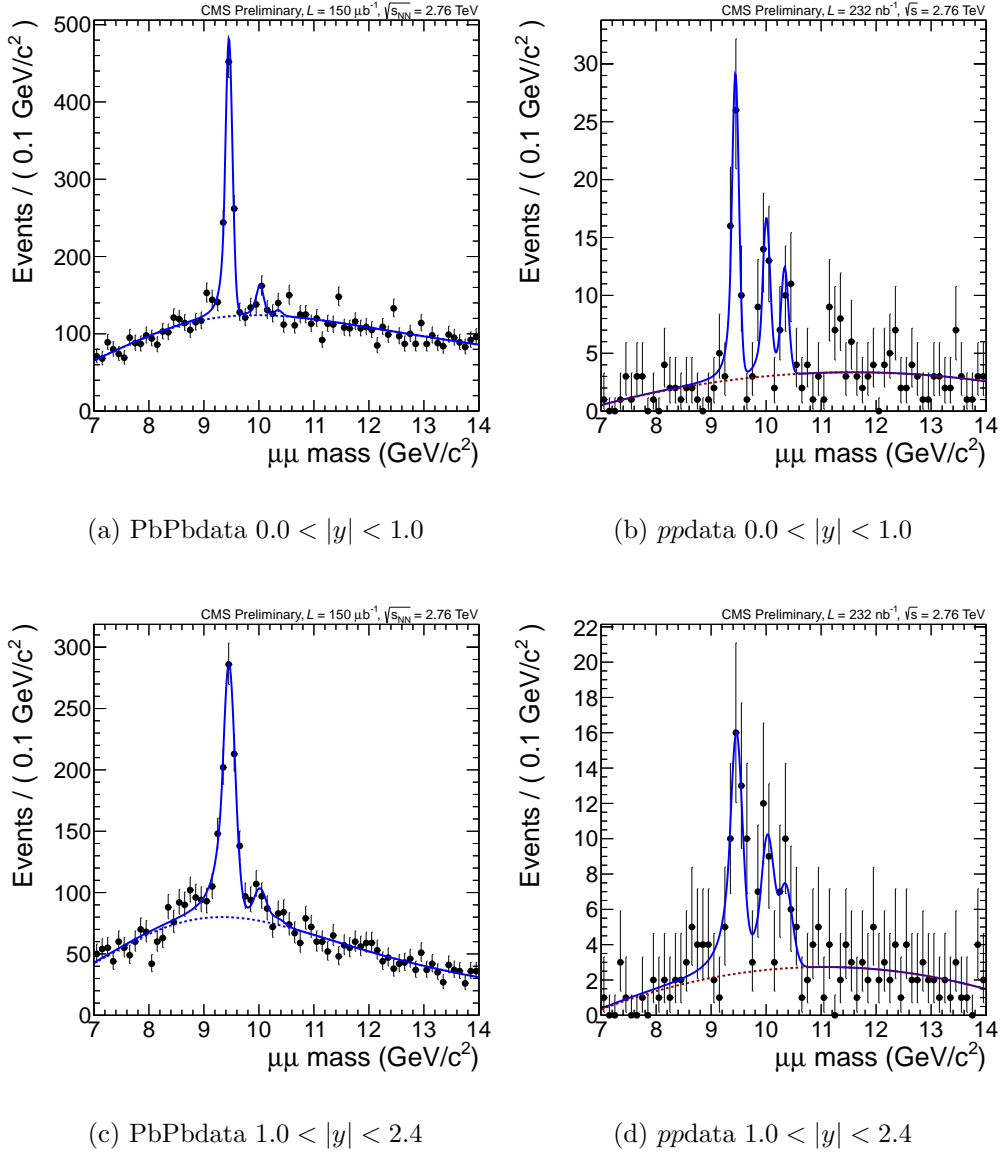


Figure 7.7: Mass fits in ranges of dimuon rapidity.

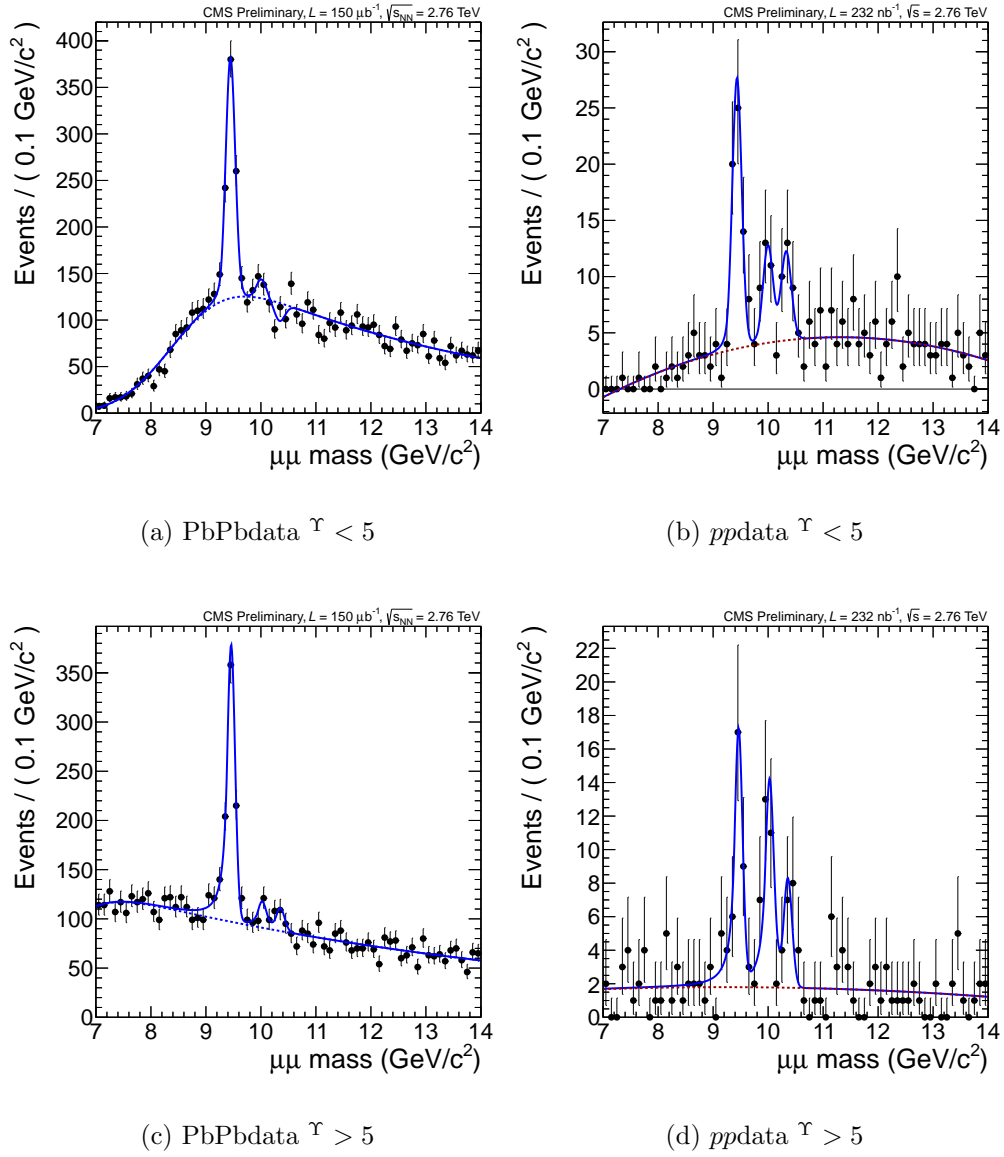
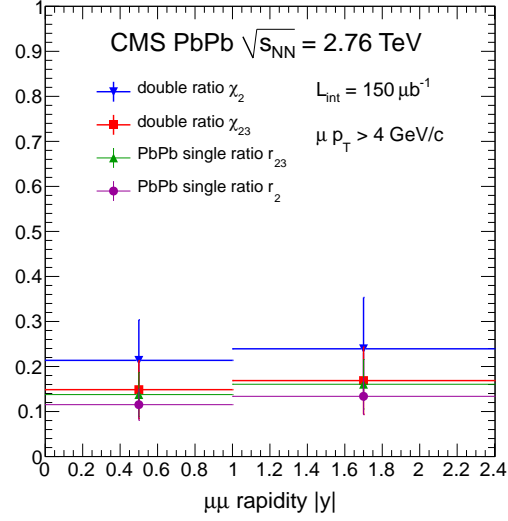
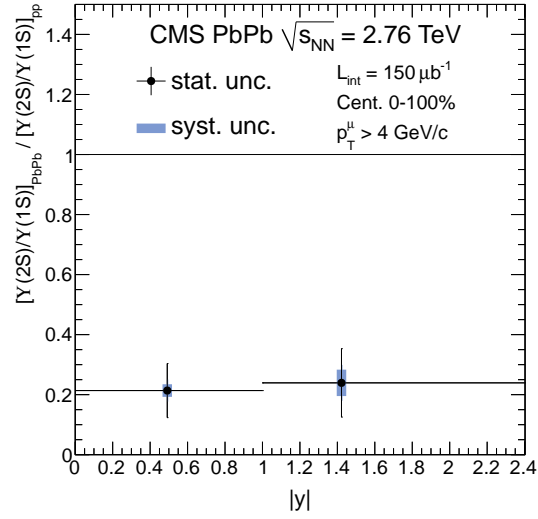


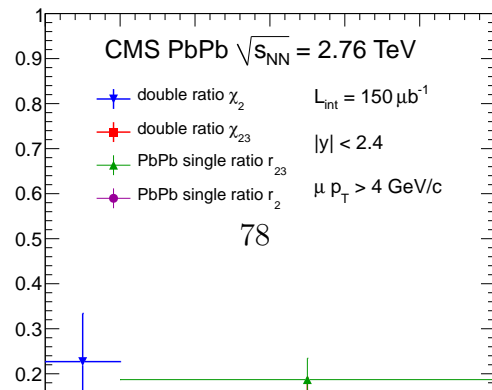
Figure 7.8: Mass fits in ranges of dimuon momentum.



(a) $|y|$ dependence, stat. err. only



(b) $|y|$ dependence, with syst.



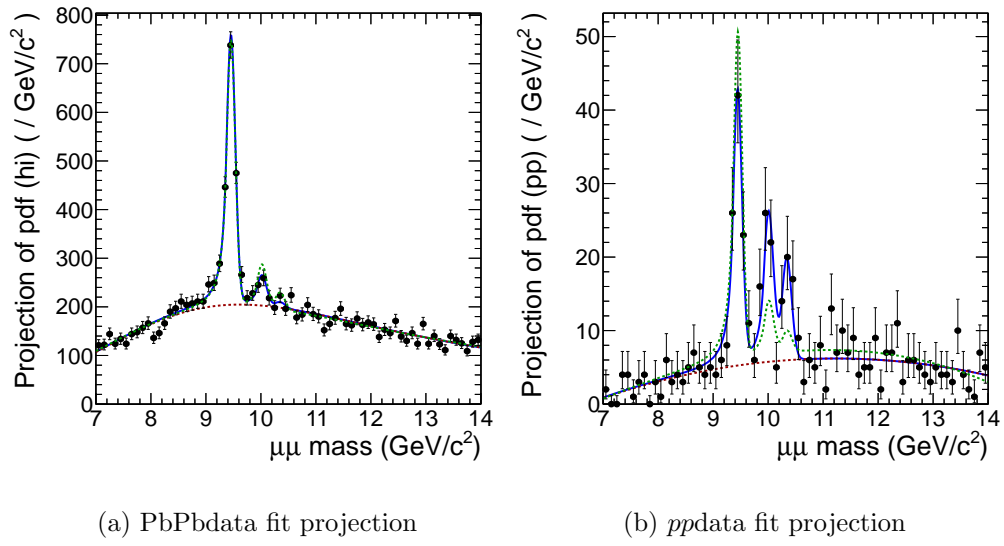


Figure 7.10: Mass projections of the fit overlaid with the same fit under the assumption of the null hypothesis show in the dashed green curve, used in the estimation of the significance.

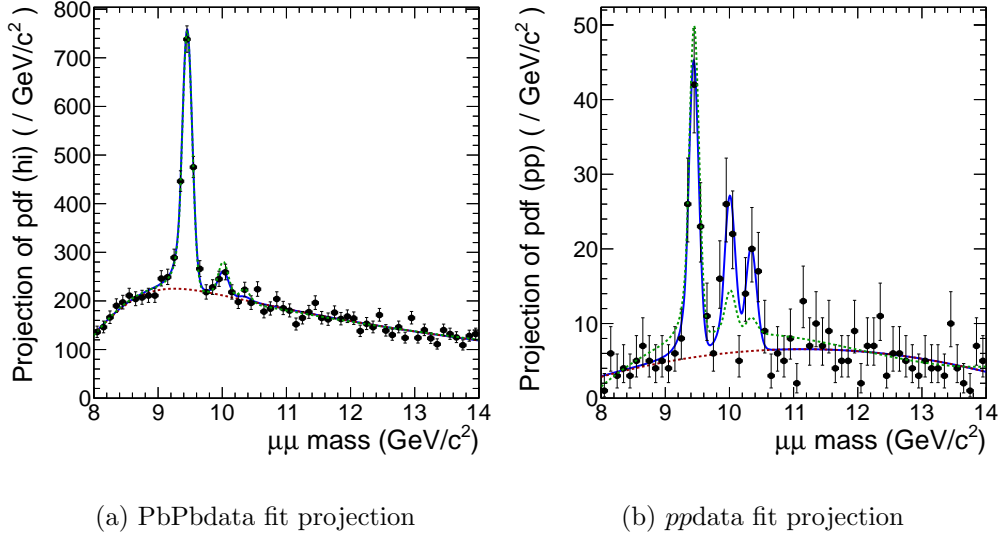


Figure 7.11: Mass projections of the fit overlaid with the same fit under the assumption of the null hypothesis show in the dashed green curve, used in the estimation of the significance; the fit is performed in a restricted mass range, as to account for the systematic and statistical uncertainties, as described in the text.

total uncertainties from the nominal fit range, including the corresponding systematic errors. We also include systematic errors on the fixed FSR tail parameter. This procedure yields a p -value estimate corresponding to 5.4σ . The projections including the null hypothesis are shown in Fig. 7.11.

For the previous measurement [?], we estimated the probability for a fluctuation of the background to yield a result as extreme as the one observed, by generating pseudo-experiments according to the no-suppression scenario (null hypothesis), and counting the fraction of occurrences (p -value) for which the double

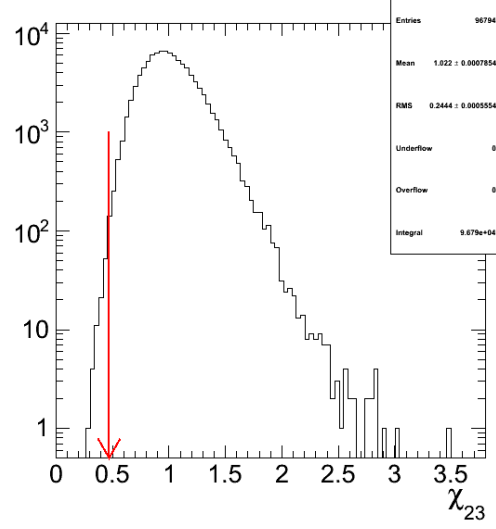
ratio value χ is smaller than that observed in the data. In further detail, the following steps are performed:

1. Take the signal and background distribution for the nominal fit. And take the background from the PbPb fit to the sidebands. In the signal shape allow for known fluctuations of the fixed shape parameters.
2. Generate a pp pseudo-data sample using the fit to the data as a template. In this, allow the relative contributions from the background and three signal resonances to shift within their respective statistics, but fix the total number of events to the number observed in data.
3. Generate background pseudo-data using the hi background model.
4. Generate the PbPb signal pseudo-data using the signal model. The number of events is constrained so that N_{bkg} (generated in step 3) and N_{sig} from this step equals the number of events observed in the data. Because we are generating this with the signal model the χ_{23} is unity up to statistical fluctuations.
5. Fit these pseudo-data samples using the nominal fitter.
6. From the distributions of χ_{23} and χ_2 obtained in this fashion, integrate from $-\infty$ to the observed data value to get the p -value of the measurement.

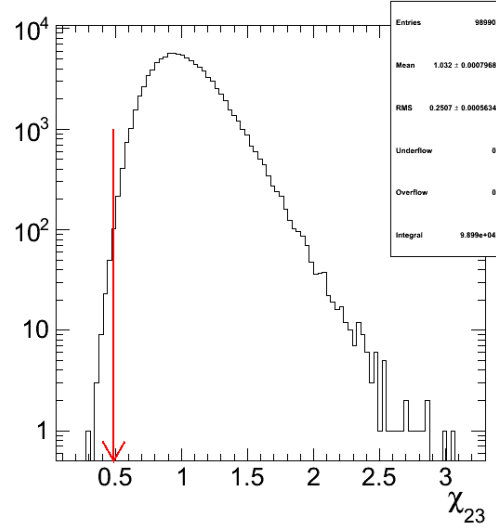
To cross-check our new profiled likelihood significance calculation we employed it on the data from the 2011 result[?]. In this, we calculated the significance using the procedure just described. When we included all systematic uncertainties we found the significance of our result was 2.4σ . Using the profile likelihood procedure with the data and models of the 2011 measurement we find a significance of 2.8σ , where this is purely statistical. The compatibility of these two methods provides some validation for the profiled likelihood significance determination.

Applying this method to half of the current data and nominal fit configuration, the distributions of χ_{23} obtained from 10k generated pseudo-experiments are shown in Fig. 7.12. The vertical, red lines indicated in the plots, at 0.472 ($\mu > 3.5$) and 0.488 ($\mu > 4.0$), denote the extracted 3σ equivalent χ_{23} values. The measured double ratio results, shown in Table 7.3, are indeed smaller than these marks, which therefore indicate a significance higher than three standard deviations.

We then generated 500k pseudo-experiments as per our outlined procedure ($\mu > 4.0$). The χ_2 and χ_{23} values were smeared from unity at generation according to their respective % systematic uncertainty. This is an extremely conservative approach since the magnitude of the error certainly doesn't scale with the central value, but since we don't know how it scales this is what we've adopted since it is conservative. This accounts for the systematic errors on the double ratios. As



(a) $\mu > 3.5$



(b) $\mu > 4.0$

Figure 7.12: Distributions of χ_{23} from pseudo-experiments generated under the hypothesis of no suppression. The arrow indicates the χ_{23} value that would correspond to 3σ significance.

shown in Fig. 7.13, there are no events with an χ_2 value as extreme as we observe. This corresponds to a p-value smaller than $2.7\text{e-}6$ which is larger than 4σ . 4σ is the limit of what we can probe with this method.

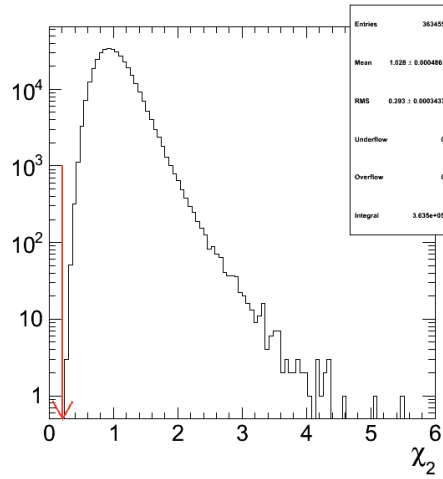


Figure 7.13: Distributions of χ_2 from pseudo-experiments generated under the hypothesis of no suppression. The arrow indicates the χ_2 value that would correspond to 4σ significance (systematic included).

Given the very small expected p-value, associated to the considerably higher significance of the current result compared to our previous measurement [?], this same method is impractical to attempt. Indeed, an estimation of the significance would require the tail of the p -value distribution in Fig. 7.12 and Fig. 7.13 to be well populated, which in turn requires larger generation of pseudo-experiments – beyond what is reasonably feasible. This justifies the usage of the alternative method described above for estimating the significance level of our current result.

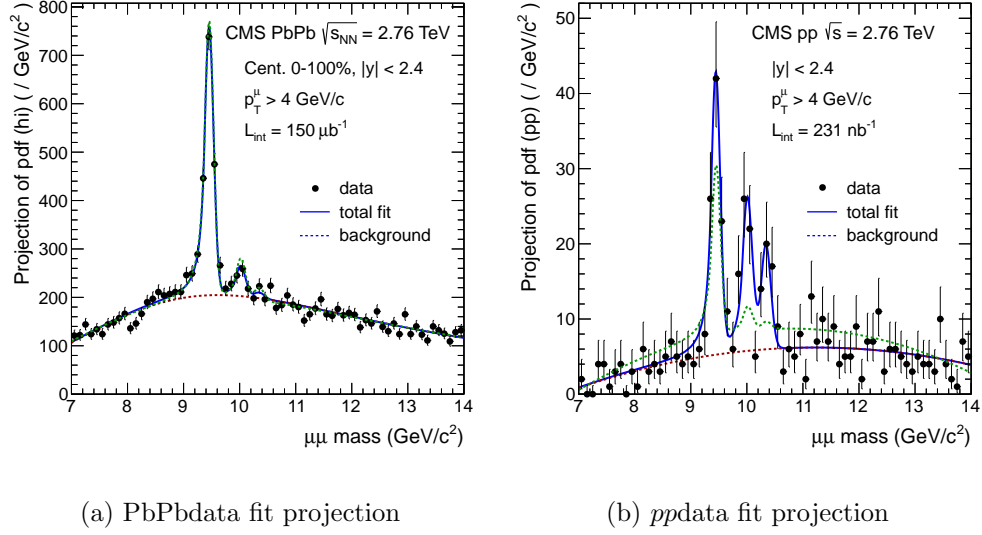


Figure 7.14: Mass projections of the fit overlaid with the same fit under the assumption of the null hypothesis show in the dashed green curve, used in the estimation of the significance. Null hypothesis: $\Upsilon(1S)R_{AA} = 1, \Upsilon(2S)R_{AA} = 1, \Upsilon(3S)R_{AA} = 1$

R_{AA} significance

Similar approach is applied to compute the significance for R_{AA} . The result is summarised in Table 7.4. The fit plots for each case are shown in Fig. 7.14, Fig. 7.15, Fig. 7.16, and Fig. 7.17.

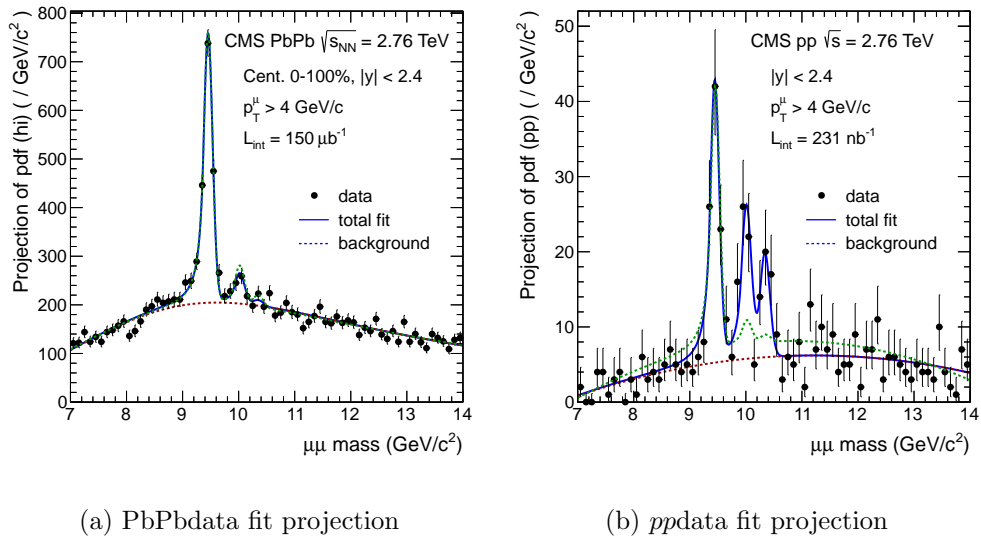
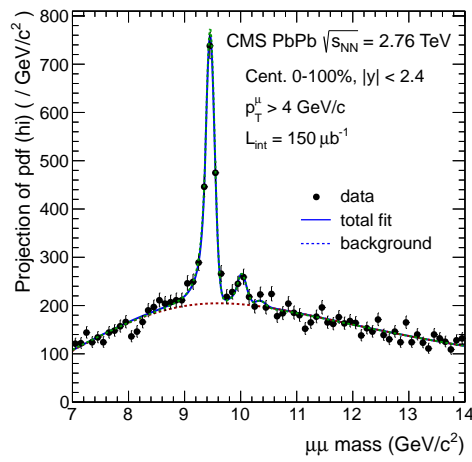
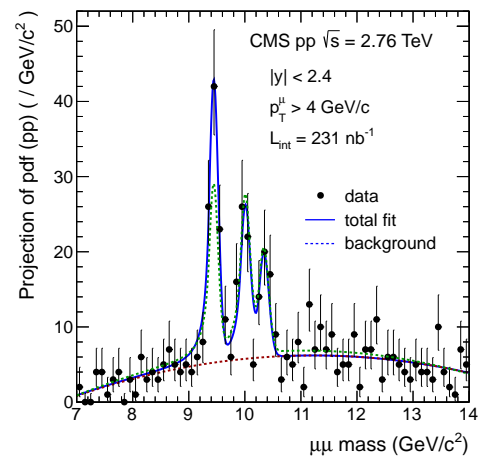


Figure 7.15: Mass projections of the fit overlaid with the same fit under the assumption of the null hypothesis show in the dashed green curve, used in the estimation of the significance. Null hypothesis: $\Upsilon(2S)R_{AA} = 1$, $\Upsilon(3S)R_{AA} = 1$



(a) PbPbdata fit projection



(b) *pp*data fit projection

Figure 7.16: Mass projections of the fit overlaid with the same fit under the assumption of the null hypothesis show in the dashed green curve, used in the estimation of the significance. Null hypothesis: $\Upsilon(1S)R_{AA} = 1$

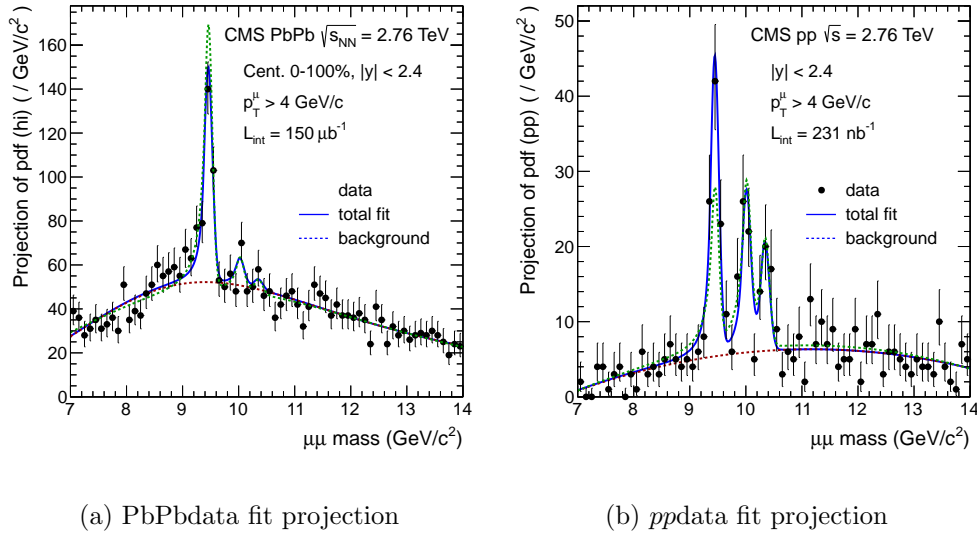


Figure 7.17: Mass projections of the fit overlaid with the same fit under the assumption of the null hypothesis show in the dashed green curve, used in the estimation of the significance. Null hypothesis: $\Upsilon(1S)R_{AA} = 1$. (*centrality* < 10% cut is used for the PbPbsample.)

Table 7.3: Double-ratio results.

		$\mu > 4.0$, Cent. 0-100%		
		χ_{23}	χ_2	χ_3
nominal result		0.15 ± 0.05	0.21 ± 0.07	0.06 ± 0.06
signal pdf systematic variations:				
fix CB tail to MC		0.135 ± 0.047	0.200 ± 0.066	0.063 ± 0.054
fix resolution to MC		0.153 ± 0.049	0.217 ± 0.070	0.081 ± 0.063
fix CB and resolution to MC		0.144 ± 0.047	0.207 ± 0.067	0.000 ± 0.000
separated floating CB tail		0.166 ± 0.052	0.226 ± 0.070	0.098 ± 0.058
separated floating resolution		0.149 ± 0.048	0.215 ± 0.070	0.080 ± 0.064
separated CB tail and resolution		0.163 ± 0.048	0.223 ± 0.064	0.098 ± 0.063
shared mean		0.150 ± 0.048	0.219 ± 0.064	0.076 ± 0.062
background pdf systematic variations:				
PbPb model	pp model			
LS erf*exp + pol.2;	pol.2	0.157 ± 0.047	0.220 ± 0.070	0.075 ± 0.064
LS keys + pol.2;	pol.2	0.161 ± 0.049	0.223 ± 0.071	0.040 ± 0.061
OS TrkRot erf*exp + pol.2;	pol.2	0.157 ± 0.047	0.221 ± 0.070	0.094 ± 0.067
OS TrkRot keys + pol.2;	pol.2	0.164 ± 0.050	0.215 ± 0.069	0.070 ± 0.062
LS keys + pol.2;	LS keys + pol.2	0.167 ± 0.053	0.234 ± 0.076	0.042 ± 0.065
LS erf*exp + pol.2;	LS erf*exp + pol.2	0.158 ± 0.048	0.222 ± 0.071	0.075 ± 0.046
erf*exp;	erf*exp	0.153 ± 0.050	0.219 ± 0.071	0.079 ± 0.068
erf*exp;	erf*exp(shared erf)	0.143 ± 0.045	0.216 ± 0.066	0.070 ± 0.062
erf*exp;	LS erf*exp + pol.2	0.148 ± 0.049	0.215 ± 0.071	0.075 ± 0.046
erf*exp;	LS keys + pol.2	0.155 ± 0.043	0.224 ± 0.063	0.081 ± 0.069
Total systematic from fit (RMS of all the fit variations):				
Fit relative systematic		7.6%	4.0%	46.8%
Fit absolute systematic		0.01	0.01	0.03
Total systematic from fit(take the largest one from equivalent variations):				
Fit relative systematic		19.3%	11.7%	100.6%
Fit absolute systematic		0.03	0.02	0.06
systematic from efficiency		1.0%	1.0%	1.0%
Total systematic:				
Total relative systematic		19.3%	11.8%	100.6%
Total absolute systematic		0.03	0.02	0.06
other checks:				
LS TrkRot erf*exp + pol.2;	pol.2	0.170 ± 0.049	0.236 ± 0.072	0.061 ± 0.080
LS TrkRot keys + pol.2;	pol.2	0.168 ± 0.048	0.232 ± 0.072	0.088 ± 0.066

Table 7.4: R_{AA} significance computed with profile likelihood ratio

null hypo	nominal fit -log(L)	null hypo fit -log(L)	significance
$\Upsilon(1S)R_{AA} = 1, \Upsilon(2S)R_{AA} = 1, \Upsilon(3S)R_{AA} = 1$	-79618.2446259	-79586.2968359	7.46σ
$\Upsilon(2S)R_{AA} = 1, \Upsilon(3S)R_{AA} = 1$	-79618.2446259	-79590.9429203	7.09σ
$\Upsilon(1S)R_{AA} = 1$	-79618.2446259	-79611.4065088	3.70σ
$\Upsilon(1S)R_{AA} = 1, \text{centrality} < 10\%$	-28215.3919703	-28204.1130248	4.75σ

Latest and older analysis results are thoroughly documented in Ref. [?]:

<http://cern.ch/cms-hin-epsilon/fitting>

hin-epsilon

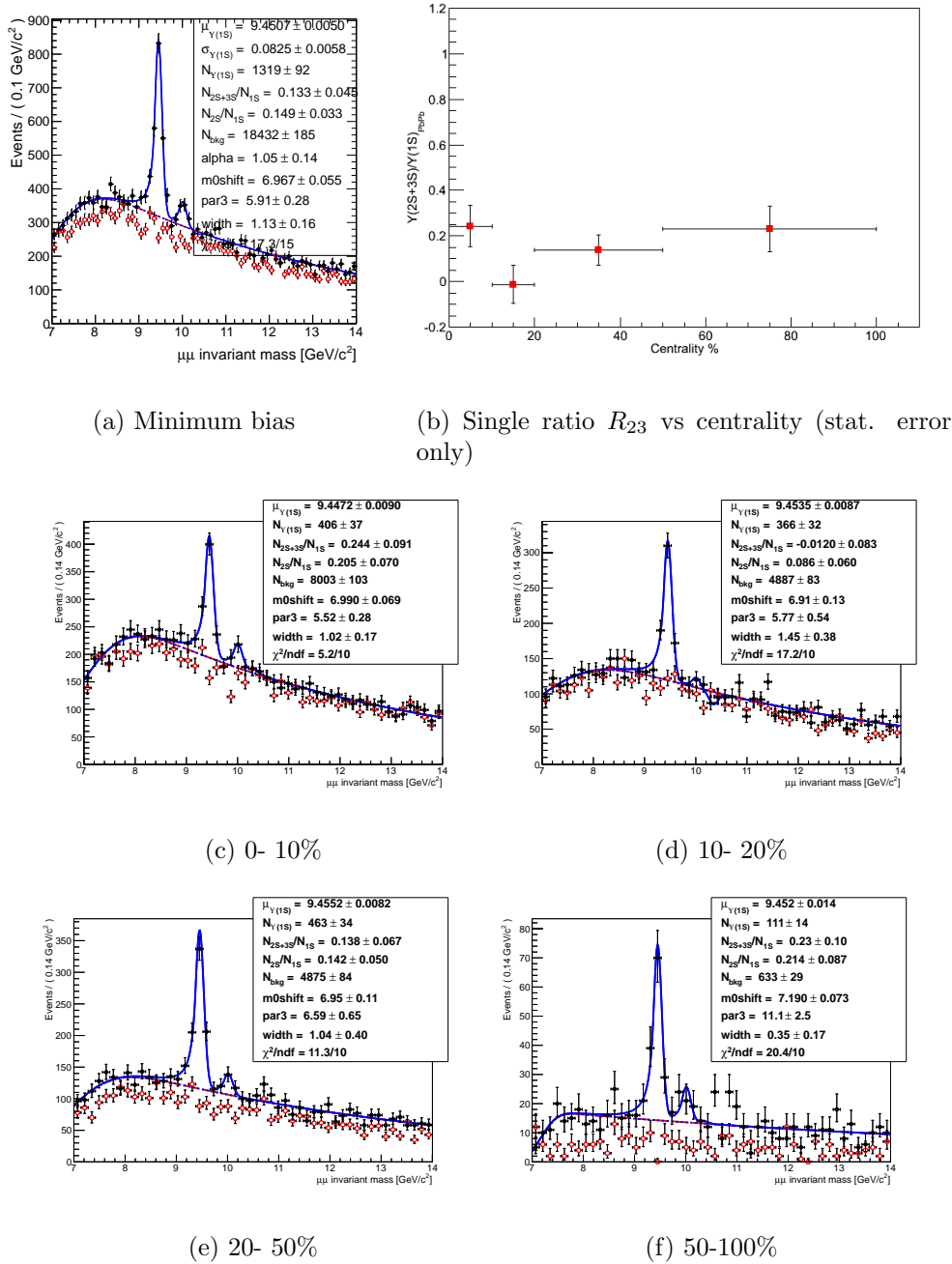
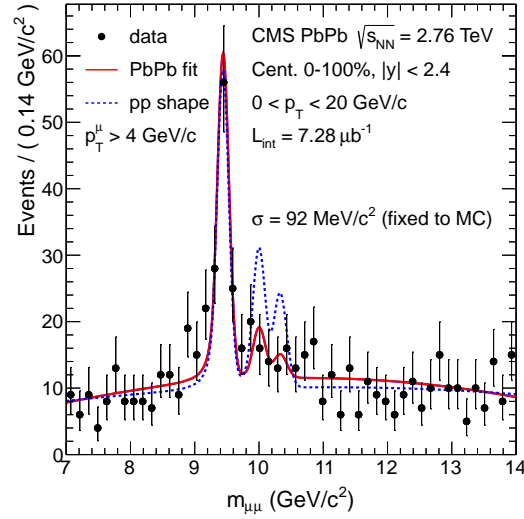
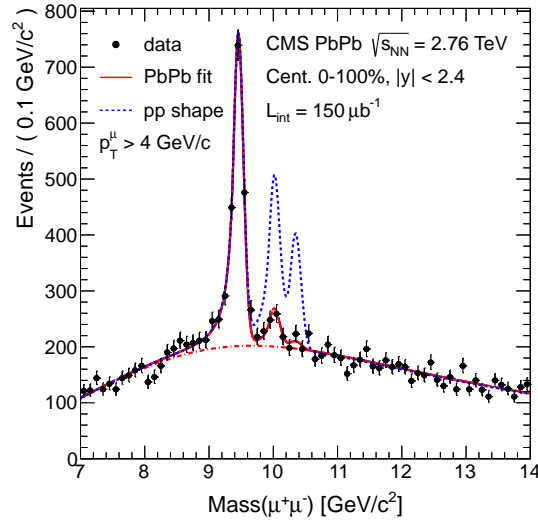


Figure 7.18: Results from the $95\mu b^{-1}$ dataset. (> 3.5)

The relative suppression of the Υ excited states has been measured, based on the first $150\mu b^{-1}$ of the 2011 PbPb dataset. The observed results ($\chi_2 \equiv 2S/1S = 0.21 \pm 0.07 \pm 0.02$ and $\chi_{23} \equiv (2S + 3S)/1S = 0.15 \pm 0.05 \pm 0.02$) are considerably more precise than, and found compatible with, the published measurements based on the 2010 PbPb dataset. Profile likelihood based estimations show the significance of the relative excited-to-ground state suppression is larger than 5σ . The larger luminosity of the PbPb dataset further allows to carry out the measurement in ranges of the dimuon kinematics and the centrality of the collision. No definitive trend is identified with the current precision. A clear dependence on the collision centrality is observed for the nuclear modification factors for the individual $\Upsilon(1S)$ and $\Upsilon(2S)$ states. The $\Upsilon(3S)$ state is not shown prominently in the PbPb data. An upper limit on the $3S/1S$ double ratio is set at 95% C.L..



(a) 2010



(b) 2011

Figure 7.19: Illustration of the excited to ground states relative Υ suppression in PbPb compared to pp , and comparison of the effect observed using the 2010 (*left*) and 2011 (*right*) PbPb datasets. The fit to the PbPb data, shown by the continuous line, is overlaid with the result of the pp fit, represented by the dashed line (shown on top of a common PbPb background shape, for comparison). For a better comparison, the background shape, background yield, mass peak width, mass peak tail shape and the $\Upsilon(1S)$ yields in the red line are fixed to the PbPb fit, while the $\Upsilon(2S)/\Upsilon(1S)$ and $\Upsilon(3S)/\Upsilon(1S)$ ratios are fixed to the pp fit values. These plots are provided for illustration, and do not reflect the analysis details.

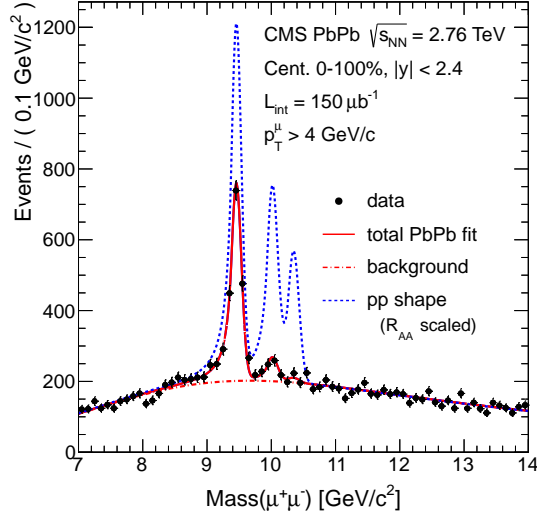


Figure 7.20: Dimuon invariant-mass distribution from the PbPb data, with the fit results shown as the solid (data + background) and dot-dashed (background-only) lines. The dashed curve illustrates the corresponding signals in pp data, scaled by the R_{AA} values. The same reconstruction algorithm and analysis criteria are applied to the PbPb and pp datasets, including a transverse momentum requirement on single muons of > 4 .

Bibliography

Bibliography

Appendices

